

Petrology of Mantle Wedge Lithosphere: New Data on Supra-Subduction Zone Peridotite Xenoliths from the Andesitic Avacha Volcano, Kamchatka

DMITRI A. IONOV^{1,2,3,*}

¹UNIVERSITÉ DE LYON, UNIVERSITÉ JEAN MONNET, F42023 SAINT-ETIENNE, FRANCE

²LABORATOIRE MAGMAS ET VOLCANS, UMR 6524, CNRS, FRANCE

³INSTITUT FÜR GEOWISSENSCHAFTEN, JOHANN WOLFGANG GOETHE-UNIVERSITÄT, 60325 FRANKFURT AM MAIN, GERMANY

RECEIVED JANUARY 16, 2009; ACCEPTED NOVEMBER 26, 2009
ADVANCE ACCESS PUBLICATION JANUARY 12, 2010

Peridotite xenoliths in arc volcanoes are very rare, usually small and remain poorly studied. Much of the earlier work focused on peridotites affected by re-crystallization, metasomatism and veining that took place shortly before the eruption of the host magmas; such lithologies may not be widespread in the mantle wedge. This study reports petrographic, major and trace element data for 17 large, fresh peridotite xenoliths from the active Avacha volcano and discusses the origin of supra-subduction zone lithospheric mantle, in particular the role and characteristics of partial melting and metasomatism. The xenoliths are spinel harzburgites containing interstitial cpx (1.5–3%) and amphibole ($\leq 1\%$). Nearly all are medium- to coarse-grained with protogranular to granoblastic microstructures; some have fine-grained domains and thin cross-cutting veins of secondary opx and olivine. Core-rim zoning and unmixing of cpx and spinel in coarse opx indicate long-term cooling to ≤ 900 – 1000°C ; $\text{Cr}\#_{\text{Sp}}$ and Al and Cr in opx are correlated with equilibration temperatures. The peridotites are highly refractory, with $\geq 44\%$ MgO and very low Al_2O_3 and CaO (0.4–0.9%), TiO_2 ($\leq 0.01\%$), Na_2O ($\leq 0.03\%$), K_2O and P_2O_5 (below detection) and REE in whole-rocks, $\leq 2.1\%$ Al_2O_3 in opx and ≤ 0.1 – 0.3% Na_2O in cpx. Comparisons of Mg, Al and Fe contents with melting experiments indicate 28–35% melt extraction at ≤ 1 to 2 GPa, in line with the absence of primary cpx and high $\text{Mg}\#_{\text{Ol}}$ (0.907–0.918) and $\text{Cr}\#_{\text{Sp}}$ (0.53–0.65). Bulk-rock Al_2O_3 is a more robust melt extraction index than $\text{Cr}\#_{\text{Sp}}$, $\text{Mg}\#_{\text{Ol}}$ and $\text{Mg}\#_{\text{WR}}$. Forearc harzburgites and certain xenoliths from the Western Pacific share many of

these characteristics with the Avacha suite and may have similar origins. A distinctive feature of the Avacha harzburgites is a combination of variable but commonly high modal opx (18–30%) with very low modal cpx. At a given olivine or MgO content, they have higher opx and SiO_2 , and lower cpx (as well as Al_2O_3 and CaO) than typical refractory peridotite xenoliths in continental basalts. These features may indicate fluid fluxing during melting in the mantle wedge. Alternatively, they could have been produced after partial melting by selective metasomatic enrichment in SiO_2 by fluids to transform some olivine into opx, although the latter mechanism is hard to reconcile with the very low alkalis and REE contents and the absence of silica correlation with fluid-mobile elements. Bulk-rock enrichments in silica and opx are unrelated to the presence or abundance of late-stage, fine-grained materials and are due to an ancient event rather than recent re-crystallization and veining.

KEY WORDS: island arc; mantle xenolith; metasomatism; spinel harzburgite; subduction

INTRODUCTION

Subduction zones are major tectonic features of the Earth and are responsible for much of its magmatic activity. It is commonly assumed that continental lithosphere (i.e.

*Present address: Université J. Monnet, F42023 Saint-Etienne cedex 2, France. Telephone: +33(0) 477481512. Fax: +33(0)477485108. E-mail: dmitri.ionov@univ-st-etienne.fr

© The Author 2010. Published by Oxford University Press. All rights reserved. For Permissions, please e-mail: journals.permissions@oxfordjournals.org

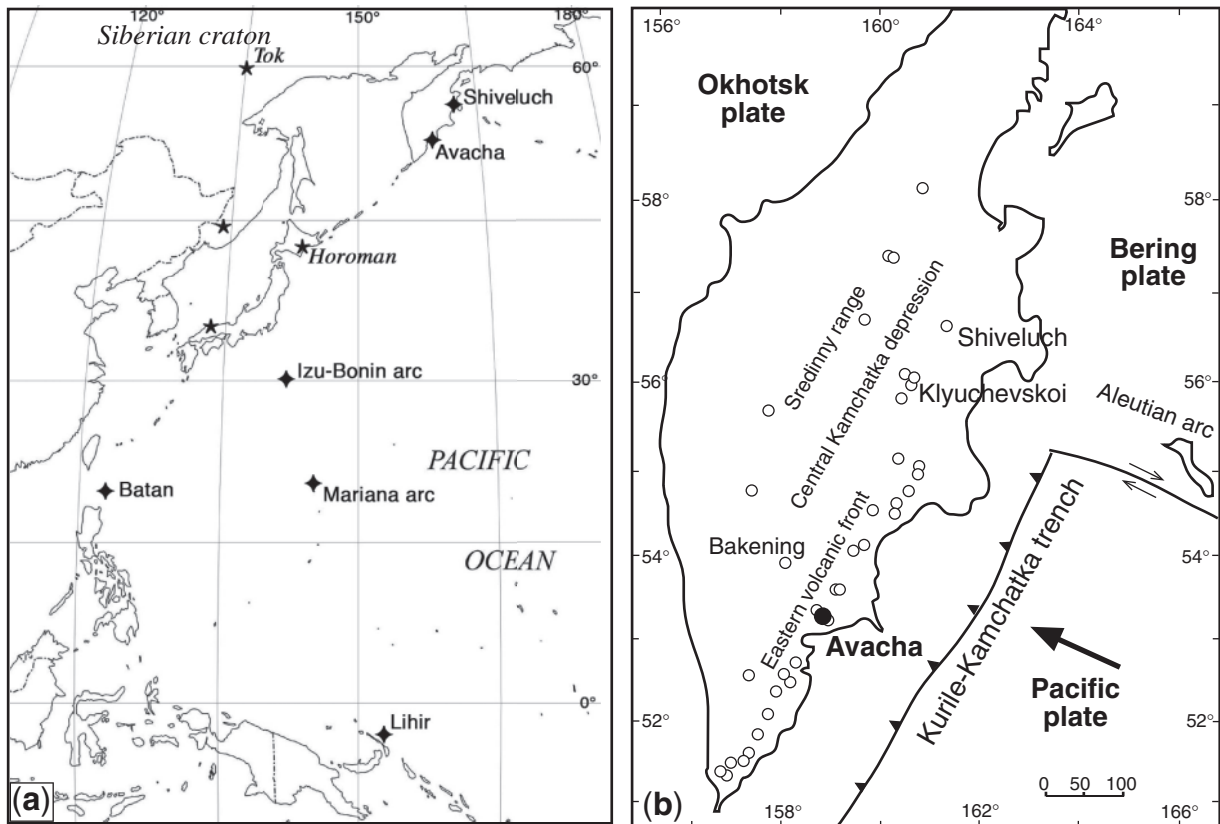


Fig. 1. (a) Location map of mantle peridotite occurrences in the Western Pacific. Samples most probably representing modern or recent mantle wedge lithosphere (xenoliths in subduction-related volcanic rocks, fore-arc peridotites from ocean drilling) are shown as rhombs. Stars show xenoliths in alkali basalts and the Horoman peridotite massif. (b) Location of major Holocene volcanoes in Kamchatka (circles) including Avacha and Shiveluch and of the Kurile–Kamchatka trench. Adapted from <<http://geo.web.ru/Mirrors/ivs/volcanoes/holocene/main/bottom2.htm>>.

lithospheric mantle and crust) can be created or profoundly transformed in island arc, convergent margin or other subduction-related environments. Key processes in those settings operate in the mantle wedge above down-going slabs, where fluids expelled from the sinking plate percolate through convecting asthenosphere to give rise to partial melting, volcanism and hydrothermal circulation (Stern, 2002; van Keken, 2003). Many petrological aspects of those processes remain poorly known because information on the mantle wedge mainly comes from indirect observations, such as studies of arc lavas, and geophysical and experimental data, which may be equivocal.

Direct samples of the mantle wedge in active island arcs can be carried to the surface by subduction-related magmas, but such xenoliths are rare and remain poorly studied. They have been reported from a small number of localities in the northern and western Pacific (Takahashi, 1980; Swanson *et al.*, 1987; Vidal *et al.*, 1989; Fig. 1a) and in the Caribbean (Parkinson *et al.*, 2003); those xenoliths can rarely yield representative whole-rock samples because of their common small size and reaction with the host magma (Takahashi, 1986; Barsdell & Smith, 1989).

Moreover, studies of such xenoliths have often focused on samples affected by re-crystallization, veining and other late-stage processes interpreted as signatures of subduction-induced metasomatism (Maury *et al.*, 1992; Kepezhinskas *et al.*, 1996; Arai *et al.*, 2003), but that may rather be due to tectonic and magma-transport effects on the lithospheric mantle. Consequently, the origin of residual or moderately metasomatized peridotites, probably the most common rock types in the shallow mantle wedge, remains poorly constrained.

Mantle samples from ancient arcs are more common but they may have been affected by processes post-dating arc formation. Valuable petrological data for an extinct (≥ 15 Ma) arc were obtained on xenoliths dredged from the ocean floor near Lihir, off Papua New Guinea (McInnes *et al.*, 2001; Franz *et al.*, 2002); however, these rocks were entrained in extension-related highly alkaline volcanic products and might have experienced more recent metasomatism in a back-arc setting. Strongly serpentinized peridotites recovered by ocean floor drilling east of the Izu–Bonin–Mariana arc (Parkinson & Pearce, 1998) represent oceanic forearc mantle (Fig. 1a).

Several studies on mantle xenoliths from the Avacha and other volcanoes near the eastern seaboard of the Kamchatka peninsula (Kurile–Kamchatka arc, Fig. 1) have been published in the last decade. Modal and whole-rock major element compositions, however, have been reported only for those from Shiveluch (Bryant *et al.*, 2007) and for a small number of Avacha xenoliths (Ishimaru *et al.*, 2007); most of the studied samples appear to be strongly affected by recent re-crystallization and metasomatism. Other publications have tackled a range of topics pertinent to mantle wedge metasomatism [trace elements, platinum group elements (PGE), Os–Pb–Nd isotopes, Li and Fe isotopes, fO_2] without providing essential petrological and other information on the samples studied (Kepezhinskas *et al.*, 2002; Arai *et al.*, 2003; Widom *et al.*, 2003; Saha *et al.*, 2005; Weyer & Ionov, 2007; Ionov & Seitz, 2008).

This study addresses the scarcity of high-quality petrological and geochemical data on typical peridotites from the Kamchatka arc and uses the new results to reassess some inferences from earlier work on the Avacha xenoliths (Arai *et al.*, 2003; Ishimaru *et al.*, 2007). It reports detailed petrographic descriptions and whole-rock and mineral major and trace element data for 17 peridotite xenoliths from Avacha, selected because of their large size and absence of reaction with the host magma or post-eruption alteration, regardless of whether they show evidence for metasomatism. Its major objective is to provide comprehensive petrological and chemical information on representative samples of the shallow lithospheric mantle in a typical modern arc setting, which may serve as an input in petrological and geophysical modelling (Soustelle *et al.*, 2010) and to better constrain its origin. Particular attention is given to sample and data quality. In addition to establishing the provenance of these peridotites I seek to highlight the chemical and textural characteristics specific to the lithospheric mantle in island arcs, to explain how those features come into being and how they are related to petrological and dynamic processes in the mantle wedge. Comparisons of these results with data for intra-plate mantle xenoliths from nearby central and NE Asia and elsewhere may help in the recognition of ‘fossil’ subduction-related mantle domains inland.

GEOLOGY AND TECTONIC SETTING

The Avacha (or Avachinsky) volcano ($53^{\circ}15'N$, $158^{\circ}51'E$; summit elevation 2741 m) is located in the southern Kamchatka peninsula near its east coast (Fig. 1), some 30 km NE of the city of Petropavlovsk-Kamchatsky. Avacha is one of Kamchatka’s most active volcanoes and is easily accessible; it formed in late Pleistocene times and recently erupted in 1991 and 2001. Its Holocene eruptions

produced ash-falls and pyroclastic flows, with compositions evolving from low-K andesite (7250–3500 ^{14}C years BP) to basaltic andesite (Braitseva *et al.*, 1998).

Avacha is located near the middle of the volcanic chain that makes up Kamchatka’s eastern volcanic front, formed 5–7 Myr ago when continuing subduction (which probably started ~ 45 Myr ago) migrated eastwards, leaving behind two older volcanic belts (Gorbatov *et al.*, 2000). There is some evidence that subduction in the area has continued even longer (since the Late Oligocene) because of the superposition of the modern arc on the older Mid-Kamchatka arc (Avdeiko *et al.*, 2002). Geophysical data indicate a double-planed seismic zone from $50^{\circ}N$ to $54^{\circ}N$ (Gorbatov *et al.*, 1997).

Avacha is situated ~ 200 km NE of the Kurile–Kamchatka trench (Fig. 1b) where the ~ 80 Ma Pacific plate is being subducted at a rate of ~ 8 cm/year, dipping at 55° . The depth to the upper surface of the slab beneath Avacha is ~ 120 km; that is, in the middle of the 90–140 km range defined for the volcanic front (Gorbatov *et al.*, 1997). The thickness of the subducted slab is ~ 70 km; slab-related seismicity can be traced to a depth of 300–400 km inland from Avacha (Gorbatov *et al.*, 1997, 1999). Seismic data indicate a crustal thickness of ~ 37 km beneath Avacha (Levin *et al.*, 2002) and the presence of shear-wave anisotropy with predominant trench-normal fast direction in the shallow mantle (Levin *et al.*, 2002, 2004). Seismic tomography shows low P-wave velocity domains beneath the Moho consistent with melt generation and volcanic activity (Gorbatov *et al.*, 1999; Manea *et al.*, 2005). Recent plate-tectonic reconstructions place Kamchatka on the Okhotsk plate (Bird, 2003; Miller & Kennett, 2006), contrary to earlier work that considered it to be on the western extremity of the North American plate (Gorbatov *et al.*, 1997; Levin *et al.*, 2002).

SAMPLE SELECTION AND PREPARATION

The xenoliths for this study were collected from volcanic ash on the western slope of Avacha, facing the Koriaksky volcano. They are angular blocks 10–40 cm in size, arguably some of the largest reported from Avacha (Arai *et al.*, 2003; Ishimaru *et al.*, 2007); some have thin coatings of the host lava or black euhedral amphibole. When split through the middle, the xenoliths have a yellowish to pink colour near the rinds (as a result of post-eruption alteration) and fresh light grey or greenish cores (Fig. 2). The coatings and altered rinds of the biggest xenoliths were removed by hammer on the spot to collect ≥ 0.5 –1 kg of the freshest core material. Smaller samples were taken as found and later sliced with a rock saw, cleaned and inspected under a binocular microscope. Xenoliths with altered cores and/or veins of host volcanic material or late-stage amphibole

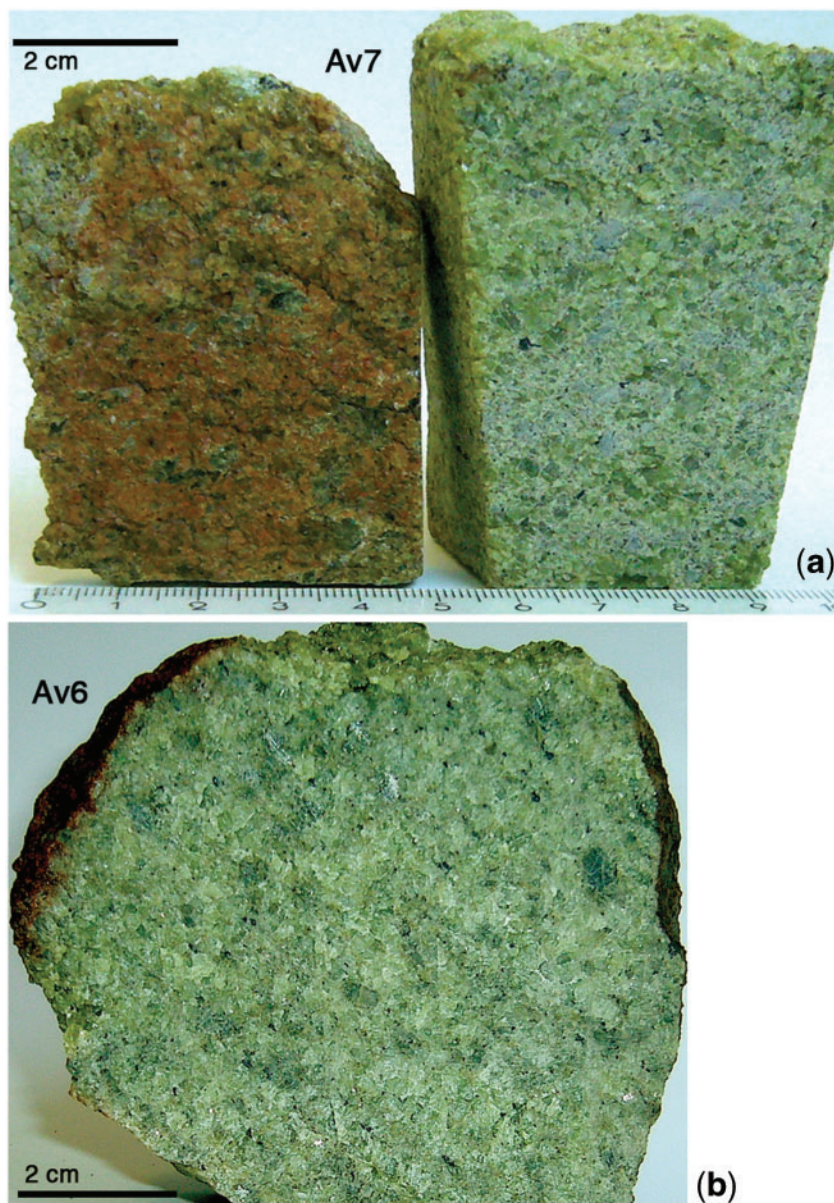


Fig. 2. Photographs of sawn hand specimens of peridotite xenoliths from the Avacha volcano. (a) Oxidized alteration crust (left) of xenolith Av7 removed to obtain alteration-free material (right) to make bulk-rock powder. (b) Xenolith Av6 has altered crust (upper left) and amphibole-rich selvages (upper right) outside but shows no apparent veining or alteration products in the centre.

were rejected. In about half of the xenoliths, the fresh core material is loosely cemented and friable; other fresh samples are solid and some have spots of darker material (Table 1). Microscopic inspection showed that the solid rocks contain fine-grained orthopyroxene (opx) cementing the coarser grained minerals; the dark grey spots are rich in the fine-grained opx.

Only homogeneous peridotites were selected for this study; that is, those that contain no macroscopically visible veins, modal gradations or centimetre-scale mineral

segregations. Overall, only three out of 20 large (≥ 10 cm) xenoliths retrieved from the sampling site were rejected because they had either coarse pyroxene-rich veins or cracks lined with black amphibole related to the outside selvages. Xenoliths Av1 and Av8 had pyroxene-rich veins near the margins, which were sawn off to make bulk-rock samples. A few samples in this study (Av1, Av8, Av12) contain very thin (barely distinguishable with a magnifying glass) more or less equally distributed veins and streaks of fine-grained materials.

Table 1: Summary of petrological data for Avacha xenoliths in this study

Sample no.	WR (g)	Hand specimen appearance	Mg#		Cr#		T (°C)		fO ₂		Calculated modal abundances (wt %)			
			ol	spl	Ca-opx	ol-spl	BBG	Wood	ol	opx	cpx	spl	am	
Av1	500	Solid, spotty	0.9104	0.582	903	950	-0.10	0.31	76.9	20.1	2.4	0.6	0.1	
Av2	510	Friable, coarse ol	0.9105	0.598	906	969	-0.30	0.18	74.8	21.1	3.1	0.6	0.4	
Av3	527	Friable	0.9094	0.643	946	950	-0.28	0.15	76.9	19.5	2.9	0.5	0.2	
Av4	150	Friable	0.9072	0.568	920	792	-0.70	-0.28	66.8	29.6	2.8	0.6	0.2	
Av5	310	Solid	0.9092	0.615	900	988	-0.37	0.08	69.6	26.7	3.0	0.5	0.3	
Av6	380	Solid	0.9102	0.654	993	995	0.02	0.49	77.3	19.8	1.4	0.6	0.9	
Av7	254	Friable to medium	0.9100	0.602	916	907	-0.76	-0.33	78.9	18.8	1.7	0.5	tr.	
Av8	310	Solid, thin f-gr. veins	0.9134	0.613	958	976	0.52	0.98	69.2	26.4	2.6	1.1	0.7	
Av9	215	Solid, whitish hue	0.9109	0.595	923	964	-0.27	0.09	79.1	18.0	1.9	0.8	0.3	
Av10	210	Friable	0.9110	0.584	949	989	0.02	0.49	73.2	23.3	2.9	0.6	0	
Av11	330	Friable	0.9118	0.643	930	914	-0.35	0.16	78.3	19.2	1.7	0.7	0.1	
Av12	325	Solid to medium	0.9110	0.562	917	978	-0.11	0.36	77.3	19.8	1.5	0.7	0.7	
Av13	210	Solid	0.9116	0.654	954	997	-0.04	0.45	76.8	19.8	1.6	0.7	1.1	
Av14	205	Friable, coarse opx	0.9109	0.545	915	972	-0.04	0.41	69.7	26.3	2.6	0.8	0.5	
Av15	200	Friable, coarse opx	0.9102	0.599	960	972	-0.55	-0.06	73.6	20.9	4.7	0.7	0.1	
Av16	155	Solid, f-gr., spotty	0.9177	0.650	989	993	1.04	1.41	76.5	20.3	2.2	0.8	0.2	
Av17	140	Friable to medium	0.9141	0.528	895	915	-0.33	0.11	79.2	18.6	1.9	0.3	tr.	

WR, weight of crushed whole-rock samples. Mg#, Mg/(Mg + Fe)_{at}; Cr#, Cr/(Cr + Al)_{at} (averages for coarse olivine and spinel). ol, olivine; opx, orthopyroxene; cpx, clinopyroxene; spl, spinel; am, amphibole. T estimates are after the Ca-opx method of Brey & Köhler (1990) based on average CaO in cores of coarse opx grains and after the ol-spl method of Ballhaus *et al.* (1991) calculated with $P=1.5$ GPa. Modal estimates are obtained by least-squares method from whole-rock and mineral analyses (see ES Table 2 for precision). fO₂ (oxygen fugacity relative to FMQ) values are after Ballhaus *et al.* (1991) (BBG) and Wood (1991) using EPMA of coarse minerals and stoichiometry to estimate Fe³⁺ and Fe²⁺ in spinel, T values from the ol-spl method of Ballhaus *et al.* (1991) and $P=1.5$ GPa.

Fresh core material (150–500 g; Table 1) was carefully crushed with a hammer between plastic sheets to <5–10 mm and inspected for extraneous materials. Splits of the crushed samples (~100 g) were ground in an agate mortar to fine powders; a duplicate bulk-rock powder was prepared from a different portion of sample Av1. Olivine, opx and spinel were hand-picked from the 0.5–1.0 mm size fractions of the remaining crushed material to produce polished grain mounts for micro-beam analysis.

ANALYTICAL METHODS

The abundances of major and minor elements in the bulk-rock samples were determined by wavelength-dispersive (WD) X-ray fluorescence (XRF) spectrometry at J. Gutenberg University, Mainz. The rock powders were first ignited for ≥3 h at 1000°C to turn all FeO into Fe₂O₃ and expel water and CO₂. Glass beads, produced by fusing 0.8 g of ignited powders with 4.8 g of dried LiB₄O₇ (1:7 dilution), were analysed on a Philips PW1404 instrument using ultramafic and mafic reference

samples as external standards. Reference samples JP-1 and UBN were analysed as unknowns to control accuracy, with results close to the recommended values (Table 2). A full duplicate analysis of sample Av1 reproduced within 0.2 wt % for MgO, 0.1 wt % for SiO₂, 0.04 wt % for FeO, ≤0.01 wt % for CaO, Al₂O₃ and Na₂O, ≤0.002 wt % for TiO₂, Cr₂O₃, MnO, NiO, K₂O and P₂O₅, and <0.0001 for Mg# [Mg/(Mg + Fe)_{at}] (Table 2). The technique was previously shown to yield improved accuracy and precision compared with conventional XRF analyses of the same samples, judging from the reproducibility of duplicates, analyses of reference materials as unknowns and less scatter on element co-variation plots (Ionov *et al.*, 2005a; Ionov, 2007; Ionov & Hofmann, 2007).

Two sets of mineral data were obtained by WD electron probe micro-analysis (EPMA). Coarse olivine, opx and spinel were analysed in grain mounts using a high-precision method designed for peridotite minerals (Sobolev *et al.*, 2005) on a Jeol JXA8200 instrument at the Max-Planck-Institut für Chemie (Mainz) using 20 kV accelerating voltage, 20 nA current and long counting

Table 2: Major oxide composition and LOI for whole-rock Avacha peridotites and reference samples

Sample	SiO ₂	TiO ₂	Al ₂ O ₃	Cr ₂ O ₃	FeO	MnO	NiO	MgO	CaO	Na ₂ O	K ₂ O	P ₂ O ₅	Total	Mg#	LOI (%)
Av1	43.65	0.008	0.50	0.392	8.11	0.136	0.323	45.56	0.71	0.019	<0.01	≤0.002	99.4	0.909	0.57
Av1d	43.75	0.009	0.50	0.391	8.15	0.134	0.321	45.77	0.71	0.007	<0.01	≤0.002	99.7	0.909	0.56
Av2	44.12	0.009	0.55	0.425	8.13	0.131	0.324	45.37	0.89	0.010	<0.01	≤0.002	100.0	0.909	0.60
Av3	43.80	0.010	0.41	0.384	8.25	0.131	0.325	45.74	0.83	0.006	<0.01	≤0.002	99.9	0.908	0.62
Av4	45.25	0.010	0.75	0.484	8.07	0.131	0.301	43.73	0.90	0.004	<0.01	≤0.002	99.6	0.906	0.56
Av5	44.91	0.009	0.63	0.413	8.02	0.131	0.313	44.56	0.86	0.022	<0.01	≤0.002	99.9	0.908	0.56
Av6	43.67	0.010	0.48	0.422	8.24	0.133	0.328	45.97	0.60	0.030	<0.01	≤0.002	99.9	0.909	0.65
Av7	43.39	0.009	0.42	0.346	8.22	0.130	0.327	46.02	0.54	0.001	<0.01	≤0.002	99.4	0.909	0.65
Av8	44.85	0.009	0.78	0.693	7.74	0.131	0.300	44.50	0.91	0.025	<0.01	≤0.002	99.9	0.911	0.53
Av9	43.35	0.009	0.50	0.452	8.20	0.131	0.328	46.19	0.58	0.009	<0.01	≤0.002	99.8	0.909	0.62
Av10	44.24	0.008	0.62	0.404	7.92	0.130	0.314	45.00	0.87	0.010	<0.01	≤0.002	99.5	0.910	0.59
Av11	43.65	0.008	0.44	0.470	8.13	0.127	0.327	46.21	0.53	0.012	<0.01	≤0.002	99.9	0.910	0.60
Av12	43.51	0.009	0.62	0.450	8.22	0.128	0.328	46.05	0.55	0.007	<0.01	≤0.002	99.9	0.909	0.61
Av13	43.85	0.012	0.53	0.452	8.12	0.132	0.325	45.90	0.64	0.026	<0.01	≤0.002	100.0	0.910	0.61
Av14	44.55	0.008	0.85	0.555	7.92	0.130	0.294	44.47	0.84	0.025	<0.01	≤0.002	99.6	0.909	0.54
Av15	44.21	0.009	0.63	0.468	7.98	0.130	0.305	44.82	1.28	0.014	<0.01	≤0.002	99.8	0.909	0.59
Av16	43.97	0.008	0.52	0.483	7.55	0.130	0.333	46.20	0.73	0.013	<0.01	≤0.002	99.9	0.916	0.55
Av17	43.63	0.010	0.50	0.268	7.83	0.123	0.331	46.54	0.55	0.003	<0.01	≤0.002	99.8	0.914	0.58
UBN (8)	45.36	0.114	3.35	0.387	8.42	0.142	0.294	40.09	1.38	0.13	0.03	0.007	99.73	0.895	-12.2
RSD (8)	0.3%	1.6%	0.6%	0.4%	0.3%	1.1%	0.2%	0.5%	0.7%	10%	17%	13%	0.3%	0.03%	
JP-1 (5)	43.71	0.011	0.71	0.429	7.61	0.121	0.325	45.92	0.56	0.02	0.01	0.004	99.42	0.915	-2.4
RSD (5)	0.3%	28%	2.6%	0.2%	0.2%	0.4%	0.3%	0.3%	2.7%				0.2%	0.02%	

Av1d, full duplicate of sample Av1. LOI, loss on ignition (3 h at 1000°C), wt % (positive values are due to oxidation of FeO to Fe₂O₃ and near-absence of secondary alteration). Values for reference samples UBN and JP-1 are averages of eight and five measurements, respectively, made on ignited powders in the same laboratory within several months before and after the analyses of the Avacha samples. RSD, relative standard deviation in % (1σ/mean).

times (120 s for peaks and background) for Ca, Al, Cr, Ni, Mn and Fe in olivine and opx. Calibration was done on wollastonite (Ca), San Carlos olivine (USNM 111312/444; Jarosewich *et al.*, 1980) (Si, Mg, Fe), rodonite (Mn) and oxides; ZAF correction was applied. The San Carlos olivine was also measured for control in duplicate after every 20–40 analyses to yield repeatability of 0.2% (1σ) for Mg and Fe, 0.3–0.4% for Si and Ni, 1% for Mn and Ca, 10% for Al and Cr, and 0.02% for Mg#. A chromite standard was repeatedly measured as an unknown for control together with the spinels.

A second dataset was obtained mainly at J. W. Goethe-Universität (Frankfurt am Main) with a Superprobe JXA-8900 at 15 kV and 20 nA, counting times of 20–40 s for peaks and 15–40 s for background, natural and synthetic minerals as standards and matrix corrections by the ZAF method. Some analyses, element distribution maps and back-scattered electron (BSE) images were obtained at the Service Microsonde Sud, Université Montpellier II on a Cameca SX-100 instrument at similar conditions. The data for olivine in this study are from the

high-precision EPMA from Mainz because grain-to-grain variations were found to be small and the repeatability for Mg#, Ni and Mn in nearly all the Avacha xenoliths is close to that obtained on the homogeneous San Carlos olivine. Averages of data from Mainz, Frankfurt and Montpellier are used for opx and spinel because grain-to-grain variations by far exceed the analytical precision of routine EPMA. The data for clinopyroxene (cpx) and amphibole (am) are from Frankfurt and Montpellier.

Modal compositions were calculated from whole-rock and mineral analyses by mass balance using least-squares regression.

Trace element analyses were made by inductively coupled plasma mass-spectrometry (ICP-MS) at the University of Frankfurt on a Finnigan Element-2 system. Whole-rock powders (~100 mg) were dissolved in HF–HClO₄ mixtures. Dried samples were taken up in HNO₃ and diluted to 1:1000 in 2% HNO₃ shortly before the analysis. Sample solutions were spiked with As, Rh and In; BHVO-1 was used for calibration. Synthetic solutions were used to correct for oxide interference. Chemical blanks

and PCC-1 and JP-1 peridotite reference materials were run with the samples. Coarse olivine and opx were analysed by laser ablation (LA) ICP-MS using a New Wave Research LUV213TM Nd-YAG laser at 10 Hz, pulse energy of 0.6–1 mJ and 120 μm spot size. USGS NIST-612 glass was used as external standard and ²⁹Si as internal standard; BIR-1g reference sample was measured for quality control.

RESULTS AND DISCUSSION

Petrography

Photomicrographs of all 17 Avacha xenoliths from this study (a full-size image of one 5 cm \times 2.5 cm thin section per sample) in plane-polarized and cross-polarized transmitted light are given in Plate 1 of the Electronic Supplement (ES) (available for downloading at <http://www.petrology.oxfordjournals.org/>). Photomicrographs of four representative xenoliths (\sim 4 cm \times 2 cm images) in plane-polarized and cross-polarized transmitted light are shown in Fig. 3; smaller-scale textural features are illustrated in Figs 4–6. Calculated modal abundances are given in Table 1 and in Table 1 of the ES (with error estimates).

All 17 xenoliths are spinel harzburgites. Their opx contents range from 18 to 30%, with consistently low modal opx (18–21%) in 12 samples. All the xenoliths contain cpx (1.4–3.1%); a higher modal cpx in sample Av15 (4.7%) is an artefact caused by irregularly distributed, coarse (\sim 1 cm) patches of poikilitic cpx, which are likely to be of late-stage origin. Spinel contents are low (\sim 0.5–1%) compared with fertile mantle peridotites (Pearson *et al.*, 2003; Ionov, 2007). All the xenoliths except Av10 contain amphibole, ranging from trace amounts to \sim 1%.

Nearly all the xenoliths are medium- to coarse-grained, with microstructures ranging from protogranular to porphyroblastic and granoblastic (Figs 3a–d and 4a). Coarse olivine and opx are usually strained and show sub-grains, preferred crystal orientation and alignment of prismatic grains and spinel clusters (Fig. 3b and d); coarse opx commonly has abundant exsolution lamellae (Figs 3d, 4c, 5d and f). Unlike the other samples, Av16 is fine- to medium-grained and mainly mosaic equigranular with subhedral, strain-free olivine neoblasts and fine-grained aggregates of anhedral opx (Figs 3e, f and 4e, f).

A specific feature of this peridotite suite is the presence in about half the samples of fine-grained domains (on a μm to mm scale) and cross-cutting veins (Fig. 3a, g and h; Plate 1 of the ES). The fine-grained domains mainly consist of secondary opx apparently produced by partial or complete breakdown and re-crystallization of coarse opx (Figs 3e, 4c–g, 5d–f and 6). The secondary opx grains are anhedral or acicular (Fig. 4d), the latter are commonly aligned with the crystal orientation or cleavage of their coarse predecessor (Figs 4c, d and 6a). Optical and BSE

images and element distribution maps show that the late-stage opx is often intergrown with cpx (brown in 4d) as well as amphibole and olivine (Figs 6). The euhedral shapes and textural position of the latter show that the fine-grained olivine (Fig. 6c and d) is not a relict mineral but rather one of the replacement products of the coarse opx. The fine-grained veins commonly consist of the same mineral as the coarse grains they cut; for example, in Fig. 3g (Av1, plane-polarized) they are light when they cut across olivine and dark grey when they cut across opx. This type of vein apparently formed by fracturing and re-crystallization of coarse olivine and opx rather than intrusion of extraneous materials. In general, samples with the most abundant veining and fine-grained pockets (e.g. Av1, Av16; Fig. 3e–h) have some of the lowest modal opx (\leq 20%), amphibole (\leq 0.2%) or cpx in the Avacha suite (Table 1).

The cpx in the coarse harzburgites occurs either in small interstitial pockets, usually in the vicinity of coarse opx (Figs 4a, 5b and 6b), or as very small anhedral grains tracing the contours of primary opx (Fig. 5b–d). The opx cores commonly contain abundant, fine cpx lamellae (Fig. 5d and f). These features link the cpx formation to unmixing of initially Ca-rich coarse opx, probably on cooling. No cross-cutting cpx-rich veins or large-scale replacement of opx by cpx (other than μm -scale grains at opx rims shown in Fig. 6a and b) is noted in the xenoliths in this study, unlike, for example, the metasomatic cpx common in mantle peridotites from the nearby Siberian craton (Boyd *et al.*, 1997; Ionov *et al.*, 2005b).

Amphibole occurs as euhedral grains in interstitial pockets and cross-cutting veins (Fig. 4h) or intergrown with cpx and opx in fine-grained pockets (Figs 5f and 6a–c), where it may have formed by reaction of metasomatic fluids with late-stage interstitial pyroxenes. Euhedral amphibole is commonly associated with empty vesicles (Figs 4h), which must have been filled with fluid during its precipitation. Olivine that hosts the am-bearing pockets has no reaction rims in contact with the vesicles (Figs 4h and 6b); in particular, it is not replaced by opx, indicating that the fluids were in equilibrium with olivine.

No phlogopite was found in any of the xenoliths in this study. Silicate glass is extremely rare; it was found only in Av6 and Av10 based on EPMA element mapping of fine-grained materials.

Mineral major element compositions

Representative microprobe analyses of minerals are reported in Table 3. Average mineral compositions are given in Table 1 of the ES; average Mg#_{OI} (Mg# in olivine) and Cr#_{Sp} [Cr/(Cr + Al)_{at} in spinel] (cores of large grains) are also listed in Table 1. All the EPMA of minerals obtained in this study are provided in Table 2 of the ES. Element distribution maps on different scales in the peridotites, coarse minerals and fine-grained pockets,

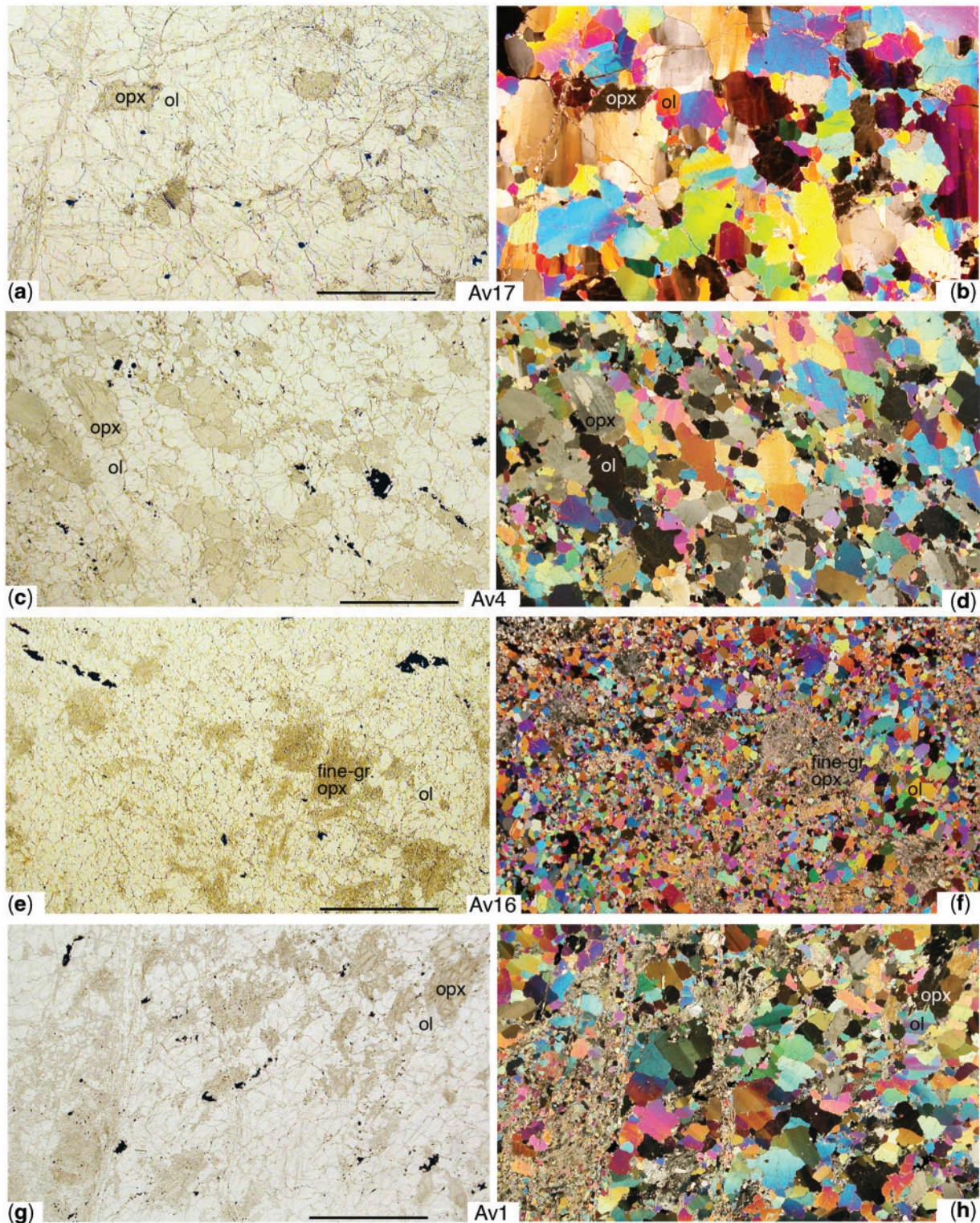


Fig. 3. Photomicrographs of Avacha harzburgite xenoliths in transmitted plane-polarized (left-hand column) and cross-polarized (right-hand column) light; field of view is about $4\text{ cm} \times 2\text{ cm}$, scale bar $\sim 1\text{ cm}$; sample numbers are indicated in the middle. The same areas are shown in the plane-polarized and cross-polarized images for each xenolith. ol, olivine; opx, orthopyroxene. In the plane-polarized images, olivine is light, coarse primary opx is olive-brown, late-stage fine-grained olivine and opx look darker and stippled, spinel is black. (a, b) coarse-grained, low-opx Av17; (c, d) medium-grained, opx-rich Av4; (e, f) fine-grained, low-opx Av16; (g, h) medium- to fine-grained, low-opx Av1 with veins and patches of re-crystallized olivine and opx. Noteworthy features are the absence of fine-grained, late-stage opx in many harzburgites (a, c), and the common preferred crystal orientation of strained olivine (b, d, h). Fine-grained veins in Av17 (a, b; left) and Av1 (g, h; centre and left) mainly consist of the same mineral (either olivine or opx) as the coarse grains they cross-cut and appear to be produced by fracturing and re-crystallization of their hosts rather than precipitation from intruded materials. Full-size ($5\text{ cm} \times 2.5\text{ cm}$) photographs of thin sections of all 17 Avacha xenoliths in this study are shown in Supplementary Data Plate 1.

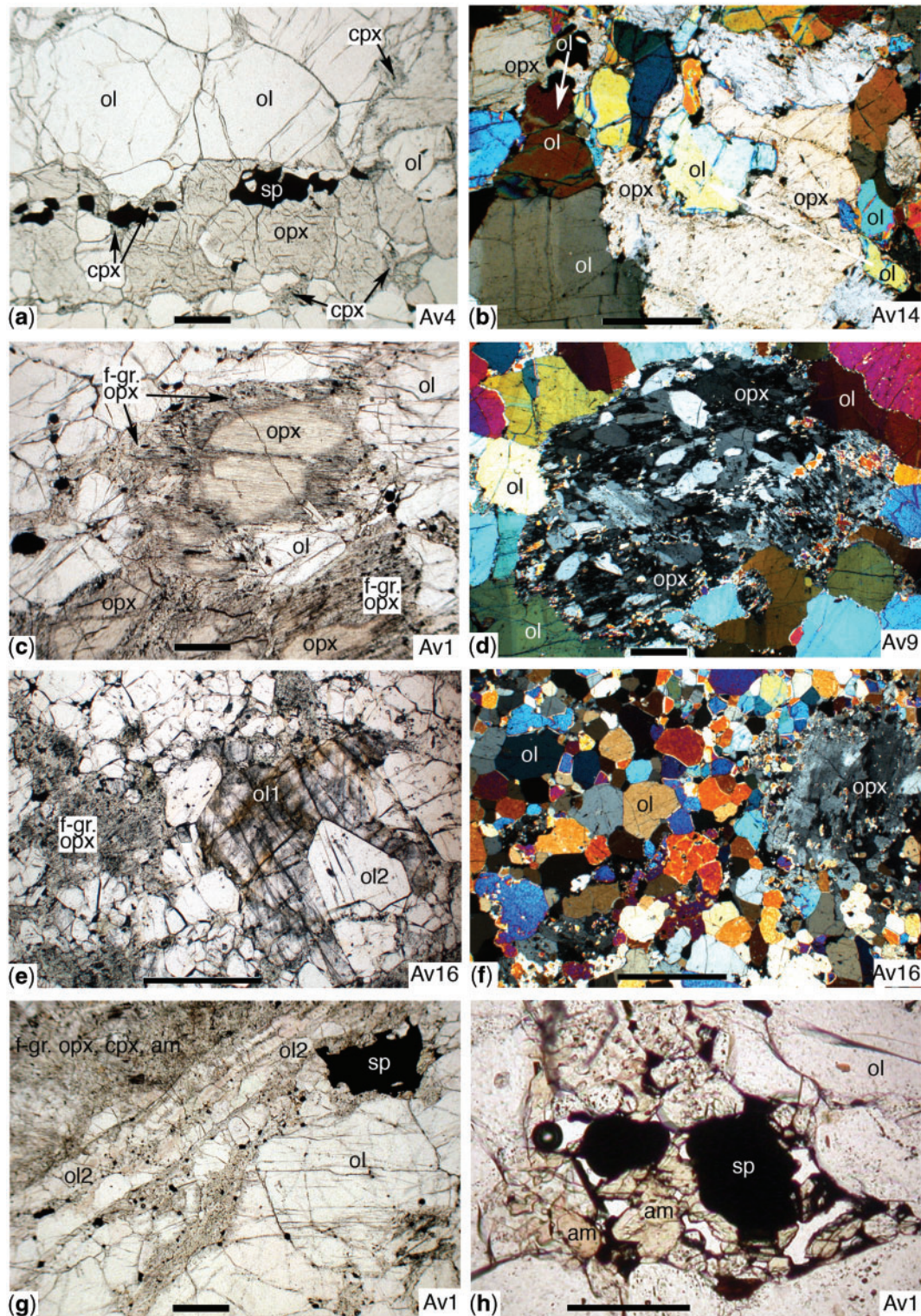


Fig. 4. Photomicrographs of Avacha xenoliths in transmitted plane-polarized (a, c, e, g, h) and cross-polarized (b, d, f) light showing the textural relations between minerals and their various generations. Scale bar ~ 0.5 mm in (a–g) and ~ 0.1 mm in (h); sample numbers are shown in the bottom right corners. (a) Coarse olivine and opx intergrown with spinel (sp) in Av4 (opx-rich); the olivine and opx commonly show triple junctions at $\sim 120^\circ$ and appear to be texturally equilibrated; rare clinopyroxene (cpx) is interstitial and occurs as small aggregates next to opx. (b) Coarse opx (grey to light yellow; centre and top left corner) containing corroded olivine in Av14; olivine grains connected with white arrows may be relics of initially contiguous, strained olivine grains partially replaced by the opx. (c) Fine-grained opx replacing coarse opx at rims and along cracks in Av1; small acicular opx grains commonly show lineation parallel to the cleavage of the coarse opx they replace; adjacent olivine has abundant cracks and fluid inclusions. (d) Coarse opx completely replaced by fine-grained opx (grey) and minor cpx (brown) in Av9. The absence of ‘fibrous’ or ‘radial’ aggregates in the late-stage opx should be noted; the most common grain shapes are prismatic and acicular. (e) Olivine neoblasts (ol2) locally replacing cloudy coarse olivine (ol1) in Av16; coexisting opx is cloudy and fine-grained and does not appear to replace any olivine. (f) Mosaic, euhedral, strain-free olivine and anhedral, fine-grained opx in Av16. (g) Detail of a cross-cutting vein in the bottom-left corner of Fig. 2g (Av1). The vein mainly consists of fragmented and re-crystallized olivine (ol2); fine-grained material next to the vein contains opx, cpx, ol, sp and amphibole (am) and may have formed after coarse opx. (h) Amphibole (am) crystals (two cleavage directions at $\sim 120^\circ$) in an interstitial pocket with empty vesicles (initially fluid-filled) in Av1. Sharp, curvilinear contacts of the vesicles with the host olivine indicate that the olivine was stable in the presence of the fluid and was not replaced by opx.

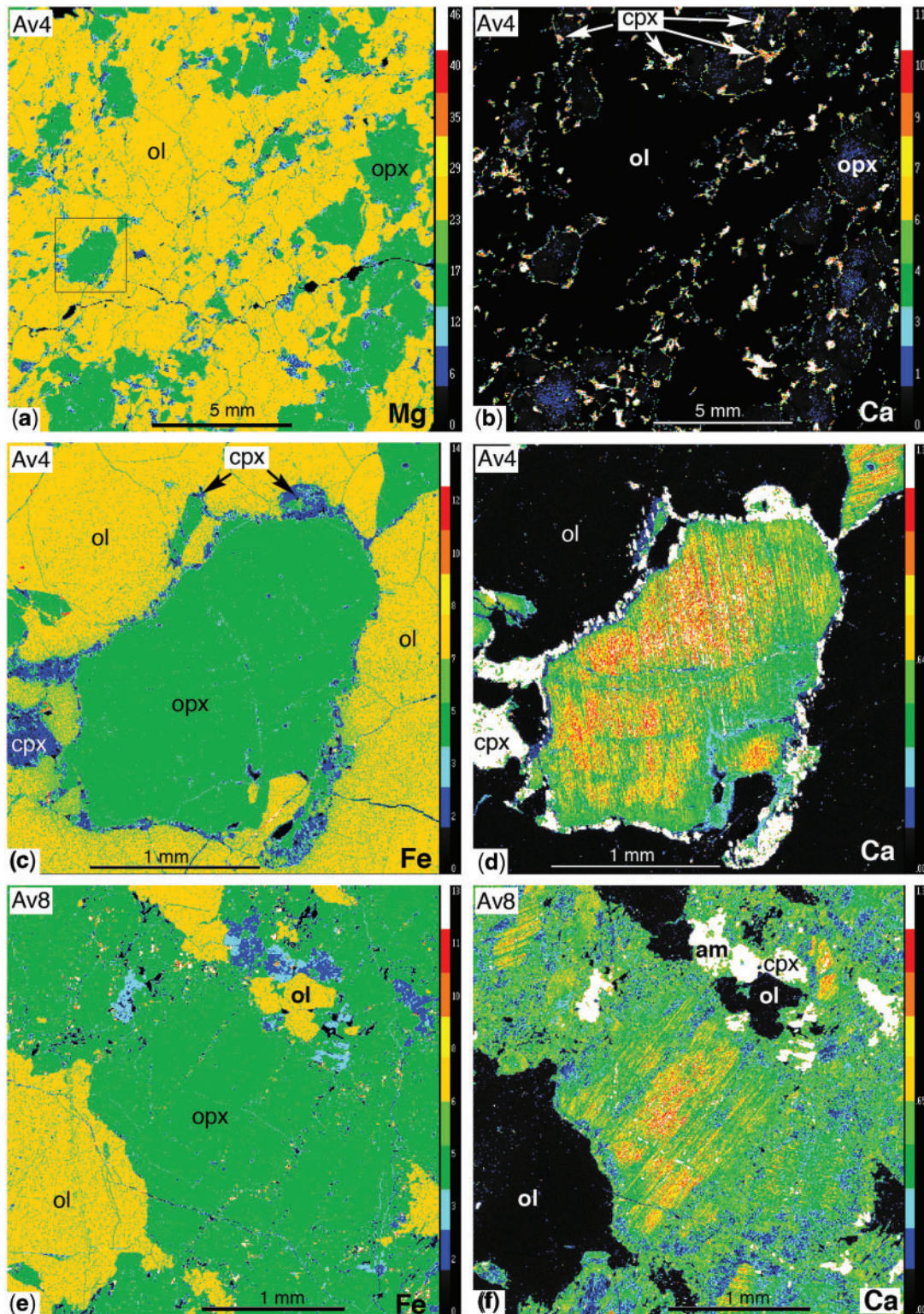


Fig. 5. Distribution maps of Mg (a), Fe (c, e) and Ca (b, d, f) in xenoliths Av4 (a–d) and Av8 (e, f) showing textural relations of cpx with opx and olivine. Abundance ranges of each element are split into 10 colour-coded intervals shown on the right of each plate, from black and blue for the lowest abundances to red and white. Cpx (low Mg and Fe, high Ca) is blue in (a, c, e) and white in (b, d, f); opx is green in (a, c–f) and black with blue cores in (b); olivine (high Mg and Fe, very low Ca) is yellow in (a, c, e) and black in (b, d, f). (a, b) Cpx occurs as small interstitial grains next to coarse opx and is uncommon between olivine grains (upper centre). The cpx does not form veins and hence is not related to Ca addition from an external source. (c, d) A close-up view of an opx grain in the centre-left of (a, b). The opx has no Fe zoning (c), but is strongly zoned in Ca (d), from 0.8–1.2% in the core (yellow to red) to 0.2–0.6% (blue and dark green) near rims and large cracks. The high Ca in the core may be due to cpx lamellae, which are too narrow to be resolved on the maps. The interstitial cpx appears to have formed mainly from Ca exsolved from nearby opx on cooling. (e, f) Fine-grained, spongy opx replaces coarse opx at rims and along fractures; coarse olivine next to the opx is intact; coarse opx has Ca-rich domains in the core and is low in Ca near rims and cracks [see also (d)]. Fine-grained opx is low in Ca (blue). Additional element distribution maps in Av4 are shown on pages 2–3 of ES Plate 2.

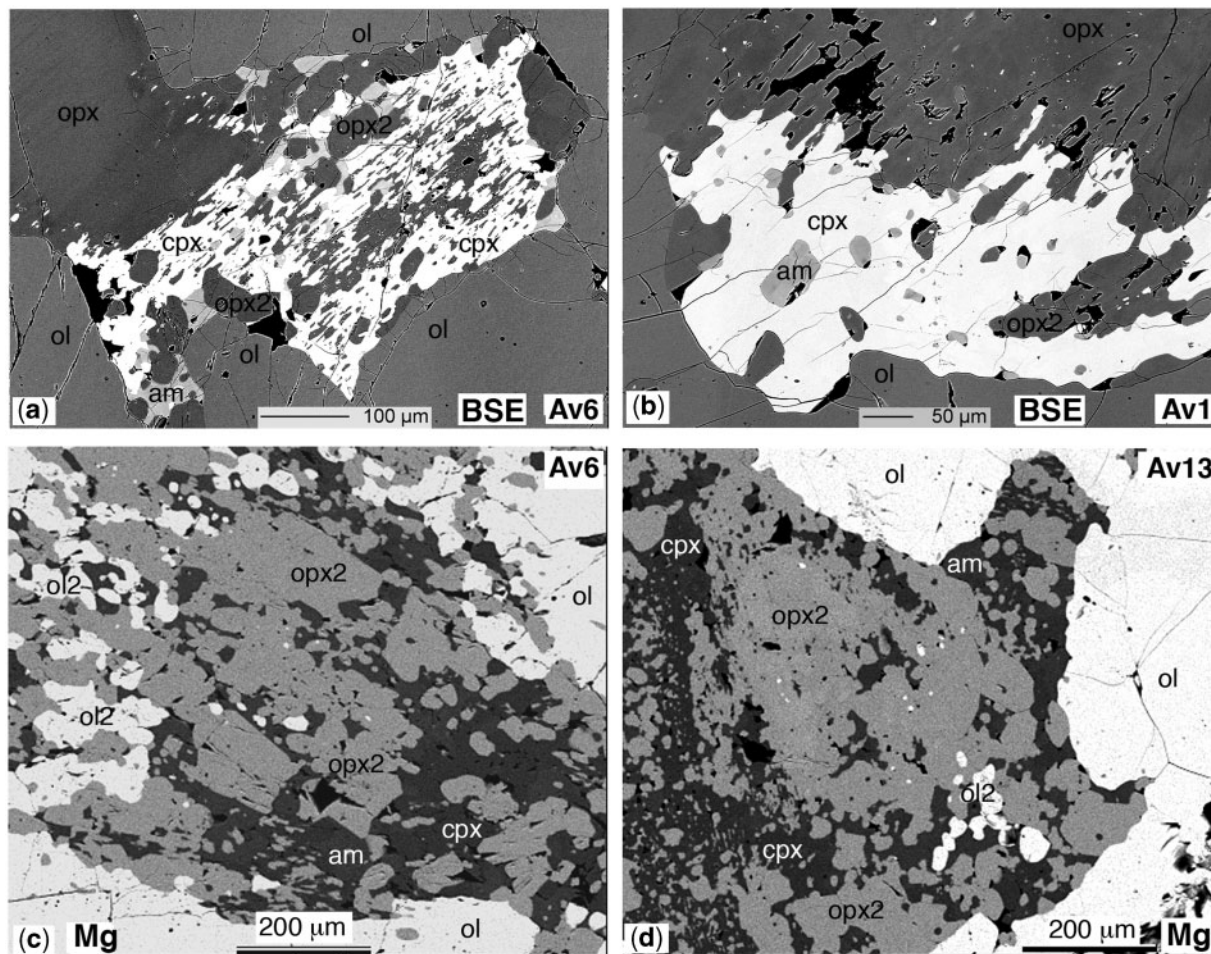


Fig. 6. (a, b) Back-scattered electron (BSE) images of Av6 and Av1 showing the textural relations of late-stage cpx (white), amphibole (am, light grey) and opx (dark grey); empty vesicles and materials lost during polishing are black. Cpx and am replace coarse opx; elongated opx relics (opx2) in (a) are parallel to the exsolution lamellae of the intact coarse opx (upper left). (c, d) Mg distribution maps in late-stage material in Av6 and Av13. In both samples, the fine-grained aggregates mainly consist of anhedral, second-generation opx (opx2), but also include newly formed, euhedral olivine (white) as well as cpx and am. Coarse olivine in (a–d) has clear-cut contacts with the late-stage aggregates. Importantly, the late-stage, fine-grained material replaces coarse opx, but not olivine. Colour distribution maps of Si, Mg, Fe, Ca and Al and a BSE image for the same area in Av4 are shown on page 4 of ES Plate 2.

obtained by EPMA, are shown in Figs 5 and 6c, d, and in Plate 2 of the ES. Mineral composition variations are illustrated in Figs 7–9.

High-precision EPMA data show that coarse olivine is homogeneous in each sample; for example, single analyses usually reproduce $Mg\#_{Ol}$ within $\leq 0.1\%$ and MnO_{Ol} within 1–2% of the averages (Table 1 of ES); that is, close to the analytical uncertainties. The high-precision analyses also allowed determination of Ca, Al and Cr (see Table 1 of ES for uncertainties). CaO contents in coarse olivine range from 0.015 to 0.04% and are positively correlated with CaO in the cores of coexisting coarse opx (Fig. 7d). The contents of Al_2O_3 ($\leq 0.003\%$) and Cr_2O_3 (0.001–0.006%) are extremely low. There is no core–rim zoning or systematic differences between coarse and

interstitial grains for olivine (Table 3, Fig. 5). By contrast, spinel rims as well as small spinel grains usually show higher FeO and wider Cr# variations than the cores of large grains (Table 3, Av17 in Fig. 7a). The $Mg\#$ of coarse spinel in all samples except one (opx-rich Av4) is negatively correlated with Cr# (Fig. 7a).

Mg in opx rims are similar to or higher than in the cores. Fine-grained opx and rims of coarse opx show wide intra-grain and grain-to-grain variations in CaO (0.1–0.9%), Al_2O_3 (0.3–2%) and Cr_2O_3 (Table 3, Table 2 of the ES). This heterogeneity suggests that some of these opx may not be fully equilibrated with cpx and spinel. Element distribution maps and EPMA data show higher Ca, Al and Cr in the cores of large opx than in the rims and near cracks (Figs 5d, f and 7b; Plate 2 of the ES).

Table 3: Representative major element compositions of minerals determined by EPMA

Olivine															
Sample:	Av1	Av1	Av3	Av4	Av6	Av8	Av8	Av12	Av13	Av14	Av15	Av16	Av16	Av17	Av17
Texture:	coarse	fine-gr	coarse	coarse	coarse	coarse	fine-gr	coarse	coarse	coarse	coarse	core	rim	coarse	fine-gr
SiO ₂	40.71	41.21	40.49	40.82	40.68	40.68	41.27	40.65	40.70	40.71	40.63	40.97	40.37	40.75	41.10
Al ₂ O ₃	0.003	0.01	b.d.	b.d.	0.002	b.d.	0.01	0.003	b.d.	0.001	b.d.	0.001	0.02	b.d.	0.001
Cr ₂ O ₃	b.d.	0.07	0.003	0.001	0.006	0.003	0.02	0.001	0.006	0.003	0.001	0.008	0.00	0.002	0.01
FeO	8.76	8.64	8.92	9.12	8.85	8.49	8.54	8.74	8.67	8.76	8.79	8.09	7.91	8.44	7.93
MnO	0.137	0.132	0.135	0.134	0.136	0.131	0.142	0.129	0.133	0.131	0.136	0.132	0.125	0.126	0.11
MgO	50.25	50.34	50.10	49.84	50.33	50.26	50.55	50.10	50.13	50.50	50.03	50.79	50.00	50.32	49.78
CaO	0.020	0.12	0.017	0.015	0.021	0.041	0.08	0.018	0.016	0.021	0.016	0.051	0.09	0.023	0.03
NiO	0.381	0.39	0.389	0.392	0.386	0.387	0.39	0.383	0.387	0.383	0.375	0.394	0.35	0.384	0.45
Total	100.29	100.9	100.08	100.35	100.44	100.03	101.0	100.06	100.08	100.54	100.01	100.47	98.9	100.06	99.4
Mg#	0.9115	0.912	0.9098	0.9076	0.9108	0.9140	0.913	0.9115	0.9121	0.9119	0.9109	0.9186	0.918	0.9146	0.918

Spinel															
Sample:	Av1	Av3	Av3	Av4	Av6	Av8	Av8	Av12	Av13	Av14	Av15	Av16	Av16	Av-17	Av-17
Texture:	coarse	coarse	fine-gr	coarse	coarse	coarse	fine-gr.	coarse	coarse	coarse	coarse	coarse	fine-gr.	coarse	small
SiO ₂	0.03	0.03	0.08	0.02	0.02	0.03	0.03	0.04	0.03	0.04	0.01	0.01	0.03	0.04	0.00
TiO ₂	0.02	0.03	0.04	0.01	0.03	0.03	0.05	0.03	0.03	0.06	0.00	0.01	0.01	0.03	0.01
Al ₂ O ₃	22.72	19.23	21.68	23.28	17.32	19.70	18.46	24.01	17.90	24.70	21.84	17.07	22.24	25.68	24.99
Cr ₂ O ₃	46.38	50.15	42.71	45.51	51.02	47.70	47.18	45.10	50.95	43.53	47.76	49.18	43.52	43.67	40.93
FeO	16.67	16.77	19.04	18.06	17.21	17.58	19.67	15.46	16.44	16.14	15.32	18.81	18.57	15.21	19.12
MnO	0.21	0.23	0.20	0.26	0.23	0.22	0.22	0.16	0.25	0.21	0.25	0.23	0.19	0.22	0.26
MgO	14.88	13.76	14.78	12.82	13.96	14.56	14.05	15.38	14.31	15.43	14.56	14.30	15.25	15.07	14.08
NiO	0.12	0.08	0.17	0.06	0.11	0.12	0.14	0.14	0.12	0.11	0.07	0.14	0.16	0.11	0.15
Total	101.0	100.3	98.8	100.0	99.9	99.9	99.8	100.3	100.1	100.2	99.8	99.8	100.0	100.0	99.5
Mg#	0.614	0.594	0.580	0.559	0.591	0.596	0.560	0.639	0.608	0.630	0.629	0.575	0.594	0.638	0.568
Cr#	0.578	0.636	0.569	0.567	0.664	0.619	0.632	0.558	0.656	0.542	0.595	0.659	0.568	0.533	0.524

Orthopyroxene															
Sample:	Av1	Av1	Av3	Av3	Av4	Av4	Av8	Av8	Av8	Av13	Av15	Av16	Av16	Av17	Av17
Position:	core	rim	core	rim	core	rim	core	rim 1	rim 2	core	core	core	rim	core	rim
SiO ₂	56.68	56.68	56.52	56.66	56.61	57.56	56.31	57.23	58.03	56.53	56.65	56.98	56.87	55.76	56.26
TiO ₂	0.01	0.00	0.06	0.00	0.01	0.00	0.00	0.01	0.00	0.01	0.00	0.00	0.00	0.00	0.00
Al ₂ O ₃	1.75	1.59	1.35	1.03	1.80	1.45	1.79	1.80	0.88	1.15	1.71	1.58	1.48	1.96	1.95
Cr ₂ O ₃	0.66	0.36	0.50	0.43	0.62	0.42	0.65	0.49	0.26	0.45	0.57	0.39	0.40	0.61	0.40
FeO	5.88	5.90	5.98	5.73	6.22	5.96	5.70	5.70	5.63	5.78	5.97	5.41	5.23	5.52	5.17
MnO	0.14	0.16	0.14	0.12	0.15	0.13	0.17	0.13	0.14	0.14	0.15	0.15	0.14	0.13	0.11
MgO	34.35	34.88	34.58	35.12	34.32	35.02	34.19	34.56	35.63	34.63	33.92	34.78	35.07	34.39	34.85
CaO	0.57	0.21	0.68	0.32	0.59	0.34	0.74	0.91	0.37	0.59	1.24	0.81	0.80	0.51	0.45
Na ₂ O	0.02	0.02	0.01	0.02	0.00	0.05	0.05	0.03	0.02	0.03	0.01	0.04	0.02	0.01	0.00
NiO	0.11	0.10	0.10	0.06	0.10	0.09	0.07	0.10	0.10	0.07	0.06	0.09	0.08	0.09	0.11
Total	100.2	99.9	99.9	99.5	100.4	101.0	99.7	101.0	101.1	99.4	100.3	100.2	100.1	99.0	99.3
Mg#	0.912	0.913	0.912	0.916	0.908	0.913	0.914	0.915	0.919	0.914	0.910	0.920	0.923	0.917	0.923

(continued)

Table 3: Continued

Clinopyroxene															
Sample:	Av1	Av3	Av4 Cpx 1	Av4 Cpx 2	Av6	Av8	Av11	Av12	Av13	Av14	Av15	Av15	Av16 exsolved	Av17 exsolved	
SiO ₂	53.34	54.39	53.08	55.16	54.19	54.75	53.79	53.68	53.34	53.98	52.80	52.03	52.99	53.74	52.77
TiO ₂	0.02	0.02	0.02	0.01	0.05	0.01	0.01	0.01	0.11	0.00	0.00	0.01	0.02	0.06	0.04
Al ₂ O ₃	1.54	0.46	2.24	1.03	1.94	1.44	1.17	1.64	1.86	1.21	2.18	1.82	1.83	1.52	2.04
Cr ₂ O ₃	0.66	0.26	0.97	0.36	0.71	0.54	0.74	0.68	0.69	0.48	1.02	0.88	0.68	0.82	0.92
FeO	2.17	1.71	1.96	1.99	2.56	2.28	2.01	2.50	2.70	2.22	1.91	1.73	2.32	1.84	1.70
MnO	0.08	0.09	0.07	0.07	0.08	0.11	0.08	0.10	0.12	0.08	0.11	0.10	0.10	0.05	0.06
MgO	17.33	18.30	17.29	18.28	17.91	17.92	17.63	17.97	17.85	18.14	17.13	16.78	17.64	17.87	17.11
CaO	23.35	23.85	24.79	24.33	23.35	24.04	23.85	22.82	22.53	23.55	24.05	23.67	22.46	23.27	24.19
Na ₂ O	0.12	0.16	0.01	0.07	0.29	0.22	0.19	0.30	0.31	0.13	0.02	0.02	0.25	0.30	0.05
NiO	0.05	0.01	0.09	0.03	0.08	0.04	0.02	0.08	0.04	0.04	0.07	0.05	0.07	0.04	0.04
Total	98.65	99.2	100.5	101.3	101.2	101.3	99.5	99.8	99.5	99.8	99.3	97.1	98.4	99.5	98.9
Mg#	0.934	0.950	0.940	0.942	0.926	0.933	0.940	0.928	0.922	0.936	0.941	0.945	0.931	0.945	0.947
Cr#	0.222	0.277	0.225	0.188	0.196	0.201	0.298	0.218	0.198	0.208	0.238	0.246	0.200	0.267	0.232

Amphibole and glass														
Sample:	Av1 Am 1	Av1 Am2	Av3 Am	Av4 Am 1	Av4 Am2	Av6 Am	Av8 Am	Av9 Am	Av11 Am	Av13 Am	Av14 Am	Av16 Am	Av17 Am	Av10 Glass
SiO ₂	46.84	50.37	47.56	56.90	53.37	46.72	46.50	49.69	50.01	46.02	46.05	46.93	48.24	60.98
TiO ₂	0.08	0.02	0.08	0.03	0.05	0.23	0.04	0.06	0.05	0.31	0.08	0.05	0.17	0.01
Al ₂ O ₃	11.23	7.72	9.81	1.51	5.99	11.32	11.10	7.92	6.97	11.85	11.51	10.96	9.12	19.86
Cr ₂ O ₃	1.90	1.70	1.97	0.37	0.91	1.61	2.17	1.57	1.47	0.53	1.24	0.74	1.87	0.03
FeO	3.80	3.14	3.33	1.83	2.43	3.99	3.82	2.92	3.20	4.15	3.87	3.70	3.41	2.64
MnO	0.06	0.03	0.05	0.04	0.06	0.07	0.05	0.06	0.06	0.07	0.07	0.07	0.04	0.05
MgO	18.57	19.55	19.65	22.96	20.56	19.47	19.30	20.57	20.76	19.32	19.42	19.82	19.73	3.89
CaO	11.99	12.08	11.80	12.99	12.62	12.19	12.06	11.95	11.96	11.82	11.83	11.78	12.39	7.10
Na ₂ O	2.28	1.84	2.04	0.16	0.82	2.15	2.12	1.67	1.47	2.49	2.21	2.36	1.49	4.21
K ₂ O	0.29	0.19	0.22	0.00	0.05	0.26	0.27	0.22	0.13	0.24	0.26	0.28	0.23	0.71
NiO	0.12	0.10	0.12	0.09	0.10	0.12	0.10	0.13	0.10	0.07	0.13	0.12	0.10	0.03
Total	97.16	96.7	96.6	96.9	96.97	98.1	97.5	96.8	96.2	96.9	96.7	96.8	96.8	99.5
Mg#	0.897	0.917	0.913	0.957	0.938	0.897	0.900	0.926	0.920	0.892	0.899	0.905	0.912	0.724
Cr#	0.102	0.128	0.119	0.141	0.092	0.087	0.116	0.117	0.124	0.029	0.067	0.043	0.121	0.001

EPMA profiles also show ubiquitous spikes for Ca, less commonly for Al and Cr (Fig. 8), produced when analysis spots overlap exsolution lamellae. Only the lowest EPMA values, which define 'plateaux' in element profiles in Fig. 8, can be considered as the true concentrations of Ca, Al and Cr in the opx cores unaffected by exsolution. Median values provided for opx cores in Table 1 of the ES are less biased towards higher Ca–Al–Cr values than averages.

Temperature estimates using Ca-in-opx (see below) should be viewed with some caution (some may be too

high) because no detailed opx profiling was done for most of the samples. The Al₂O₃ in the cores of large opx is positively correlated with Cr₂O₃ (Fig. 7b and c); in contrast, both Al and Cr show negative correlations with Ca (Fig. 7c).

The xenolith suite shows significant variations in Mg#_{OI} (0.908–0.918) and Cr#_{Sp} (0.53–0.66), but no statistically meaningful correlation between these two parameters (Fig. 7e), which are commonly considered as melt extraction indices. The Mg# is negatively correlated with

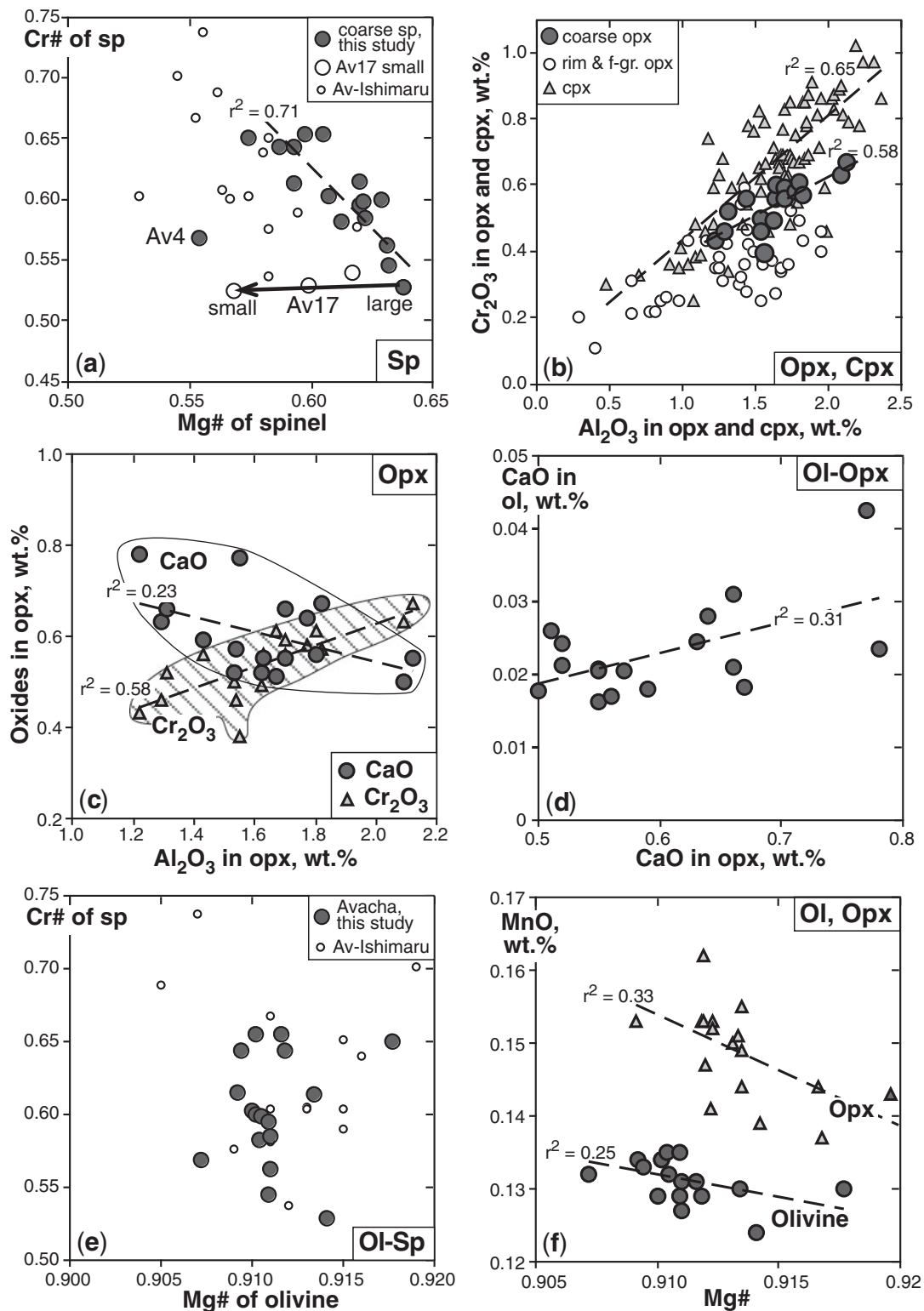


Fig. 7. (a–f) Co-variation plots for mineral compositions in the Avacha peridotites from this study [data from ES Table 1 and from Table 2 for (b)]; dashed lines are linear correlations, r^2 values are correlation coefficients. Also shown in (a) and (e) are data for Avacha xenoliths reported by Ishimaru *et al.* (2007) (small open circles). Spinel and opx compositions are related to their textural position as shown by Fe-enrichment in fine-grained relative to coarse spinel in Av17 (a) and lower Al and Cr in opx rims than in cores (b). No positive correlation between $Mg\#_{ol}$ and $Cr\#_{sp}$ is seen in (e), although both parameters are often viewed as robust melt extraction indices. In contrast, the negative $Mg\#$ -MnO trend in olivine and opx (f) must be related to melt extraction.

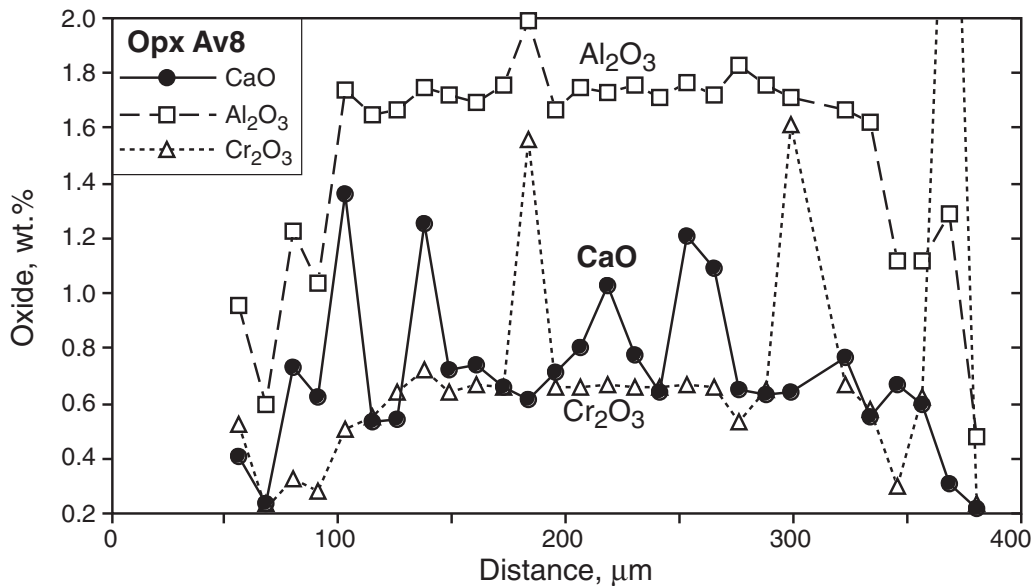


Fig. 8. Contents of CaO, Al₂O₃ and Cr₂O₃ (wt %) measured in a profile across a coarse opx in Av8 shown in Fig. 5e–f (ES Table 2). The bumpy concentration profiles are partly due to exsolution lamellae of cpx and spinel. The true ‘baseline’ CaO content of the opx core may be indicated by the ‘plateau’ of lowest values ranging from 0.5 to 0.7% CaO; a fair approximation may be provided by a median (i.e. discarding outliers) rather than an average of the analyses.

MnO in olivine and opx (Fig. 7f); in contrast, Mg#_{O1} is not correlated with NiO_{O1}.

The cpx are diopsides with very low Al₂O₃ (1–2.4%), TiO₂ (≤0.04%) and Na₂O (0.01–0.35%), moderate Cr₂O₃ (0.3–1.0%), and high CaO (22–25%) and Mg# (0.92–0.95) (Figs 7b and 9a, b). In spite of some grain-to-grain variations, their compositional ranges are specific for each xenolith; for example, >100 electron probe micro-analyses of cpx in Av4 yielded Na₂O and TiO₂ ≤0.03% and Al₂O₃ from 1.6 to 2.2%. For single cpx grains, Al is positively correlated with Cr (Fig. 7b), Al and Cr show no meaningful correlations with Ca and Na, and Na is negatively correlated with Ca and Mg# (Fig. 9a and b). For average cpx compositions in each xenolith, there are no correlations between Mg# in cpx and olivine, Cr# in cpx and spinel, or Al₂O₃ in cpx and coarse opx, which may indicate incomplete equilibration of the late-stage cpx with the coarse minerals and thus affect temperature estimates from the two-pyroxene and cpx–ol geothermometry methods.

Ishimaru *et al.* (2007) and Ishimaru & Arai (2008) characterized amphiboles in their xenoliths from Avacha as calcic and identified tremolite, edenite, pargasite and hornblende. EPMA data on amphiboles from this study can be interpreted in terms of compositional continuity between two chemical end-members (Fig. 9c–f): (1) one with high Al₂O₃ (10–12%), high Na₂O (2–2.5%) and low Mg#, and (2) a high-Mg# (>0.95) end-member low in Al₂O₃ (~2%), Na₂O (<0.5%) and K₂O (≤0.05%) similar to

tremolites reported by Ishimaru & Arai (2008). The total amphibole population displays negative Mg#–Al and Mg#–Na and positive Mg#–Ca (Fig. 9c) and Na–K (Fig. 9f) correlations. The Na–Al-rich amphiboles are more common whereas the tremolites occur in only few xenoliths and often coexist with (Al,Na)-poor cpx. Ti contents are very low (mainly <0.1% TiO₂) and are poorly correlated with K (Fig. 9e). The low Ti and K distinguish the Avacha amphiboles from those in other off-craton mantle xenoliths worldwide (Ionov *et al.*, 1997; Coltorti *et al.*, 2007; Ishimaru *et al.*, 2007). Cr and Al show a good positive correlation in the majority of the amphiboles except for a subset of Al₂O₃-rich (>10%) amphiboles, which shows wide variations in Cr₂O₃ (2.5 to <0.5%; Fig. 9d). The Cr-rich amphiboles in Fig. 9d appear to be equilibrated with spinel, like those shown in Fig. 4h, but this may not be the case for the Cr-poor amphiboles that plot off the main Cr–Al trend. Average Mg# in coexisting cpx and the Al-rich amphibole in each xenolith are positively correlated ($r^2=0.5$), indicating common chemical equilibration between these two interstitial minerals; by contrast, Mg# values either in amphibole or in cpx are not correlated with the Mg# of coarse olivine. EPMA data using high counting times yielded 0.07–0.10% F in amphibole Av2 and ≤0.03% F in Av4 and Av8; Cl is below detection limit.

Temperature, pressure and fO_2 estimates

Equilibration temperatures (T) were estimated using the Ca–opx method of Brey & Köhler (1990) and the

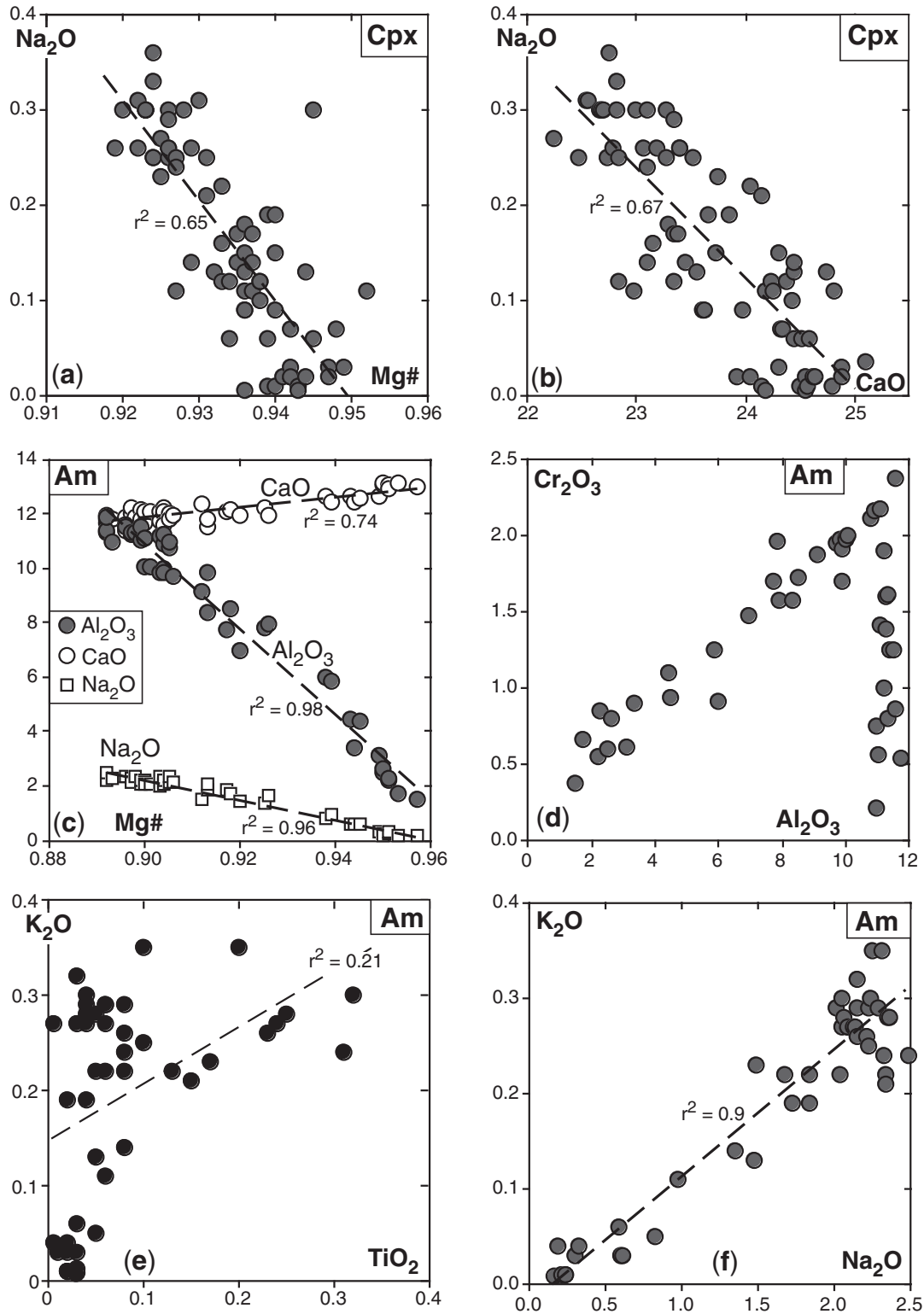


Fig. 9. Co-variation plots for EPMA data for cpx and amphibole in Avacha peridotites from this study (ES Table 2). The cpx are very low in Na and rich in Ca (a, b). The amphiboles define a continuous series between the edenite and the tremolite end-members; the low-Na,Al tremolites have much higher Mg# than the edenites (c). The Al-rich amphiboles show a wide range in Cr (d) probably related to variable degrees of equilibration with Cr-rich spinel. The amphiboles, in particular the tremolites, are low in K and Ti; the contents of K and Ti are poorly correlated (e).

ol-opx-sp method of Ballhaus *et al.* (1991), based on the average compositions of cores of large grains from Table 1 of the ES and assuming a pressure of 1.5 GPa. The T estimates are given in Table 1; these range from 895 to 993°C for the Ca-opx method and from 907 to 997°C for the ol-opx-sp method (except an 790°C outlier for Av4 with a spinel composition that plots off the Cr#–Mg# trend defined by the remainder of the samples in Fig. 7a).

Two-pyroxene, Ca-opx and Ca-olivine thermometry assume that cpx, opx and olivine coexist in a rock and are in equilibrium with respect to Ca (Brey & Köhler, 1990; Köhler & Brey, 1990). This may not be evident for the Avacha xenoliths because cpx is a late-stage mineral, and coarse opx and olivine grains may not be fully equilibrated with the rare interstitial cpx. However, the correlation between CaO in opx and in olivine (Fig. 7d) as well as the ubiquitous spatial association of coarse opx with cpx (Fig. 5) suggest Ca equilibration (at least partial) between these minerals. Another strong argument for the validity of the Ca-opx T estimates is that they define the same T range as the ol-opx-sp method (Table 1). Overall, the temperatures from the two methods appear to be realistic and correspond to a stage of cooling in the lithospheric source of the xenoliths.

It is less clear if cooling continued below the T estimates obtained from the cores of large olivine, opx and spinel grains. The rims of coarse opx are commonly lower in Ca than the cores (Figs 5 and 8) implying lower equilibration temperatures; however, the rims locally also have higher Ca (Av8 in Table 3). Ca distribution in late-stage interstitial opx is very heterogeneous with wide intra-grain and grain-to-grain variations (Table 2 of the ES). These results can be qualitatively interpreted in terms of two successive events. (1) The cooling in at least some of the samples in this study may have continued below the T values recorded in the cores of large opx and spinel. (2) Infiltration of metasomatic fluids, veining and recrystallization that precipitated amphibole and produced fine-grained materials shortly before (and during?) the entrainment of the xenoliths into the host magma may have been accompanied by localized heating. Possible partial re-equilibration to higher T may be recorded in the most fine-grained and re-crystallized xenoliths, such as Av16 (Table 1).

Temperature estimates from CaO in coarse olivine after Köhler & Brey (1990) at 1.5 GPa and using empirical calibrations based on equilibrated spinel peridotite suites (Ionov, 2007) yield low T values (~ 800 – 900 °C); however, these estimates have large errors. Nevertheless, the very low CaO (mainly $0.020 \pm 0.005\%$), Al_2O_3 ($\leq 0.003\%$) and Cr_2O_3 (0.001 – 0.006%) in the Avacha olivines compared with those in other shallow mantle peridotites (Ionov *et al.*, 2005c; Witt-Eickschen & O'Neill, 2005; Ionov, 2007) may be considered to indicate fairly low

ambient temperatures at the end of the lithospheric cooling (Köhler & Brey, 1990).

Equilibration pressures cannot be established because of the absence of reliable P – T methods for spinel peridotites, but they can be assessed qualitatively from observations on websterite and other types of pyroxenite veins in the Avacha xenoliths. Such veins from this collection and those previously reported by Arai *et al.* (2003), Ishimaru *et al.* (2007) and Ishimaru & Arai (2009) do not contain either garnet or plagioclase and thus probably equilibrated at 1.1 – 2 GPa $\leq P \leq 1.6$ – 1.8 GPa based on experimental studies (Webb & Wood, 1986) and observations on veined garnet–spinel xenolith suites (Ionov *et al.*, 1998).

$f\text{O}_2$ values [oxygen fugacity relative to the fayalite–magnetite–quartz (FMQ) buffer] were calculated after Ballhaus *et al.* (1991) and Wood (1991) using average EPMA data for cores of coarse minerals, Fe^{3+} in spinel estimated from stoichiometry and assuming a pressure of 1.5 GPa. The $f\text{O}_2$ estimates are listed in Table 1. Those after Wood (1991) are somewhat higher, but, in general, both methods yield higher $f\text{O}_2$ values for the Avacha xenoliths than for abyssal peridotites and the majority of intra-plate peridotite xenoliths (Bryndzia *et al.*, 1989; Ionov & Wood, 1992) as reported earlier by Ishimaru *et al.* (2007). $f\text{O}_2$ estimates obtained using spinel rim compositions (Table 3) are 1 – 1.5 \log_{FMQ} units higher than for the spinel cores, indicating highly oxidized conditions during the recent metasomatism and re-crystallization.

Whole-rock major element compositions

Whole-rock compositions determined by XRF and loss on ignition (LOI) data for 17 Avacha xenoliths are given in Table 2 and in Table 1 of the ES. The LOI values range from $+0.53\%$ to $+0.65\%$ and are positively correlated with total iron as FeO (Fig. 10a). The gain of mass on ignition means that oxidation of FeO to Fe_2O_3 is more significant than the loss of volatiles (usually H_2O and CO_2 from alteration products) if they are present. The LOI values are only slightly lower than the highest possible mass gain of $\sim 0.8\%$ for a fresh peridotite with 8% FeO; moreover, some iron must be in the form of Fe^{3+} in spinel, pyroxenes and amphibole. The FeO–LOI trend in Fig. 10a is roughly consistent with the theoretical rate of increasing mass gain on ignition with higher iron contents. Overall, the LOI data show that secondary alteration is nearly absent in the Avacha peridotites in this study, in line with petrographic observations.

Co-variation plots for major oxides in the Avacha xenoliths are shown in Figs 11 and 12 together with compositions of residues of melt extraction from fertile lherzolites at 1–5 GPa from experimental data (Walter, 2003; Herzberg, 2004). Figure 11 compares the Avacha suite mainly with off-craton continental peridotites and xenoliths from ocean islands, whereas Fig. 12 addresses its relations with other supra-subduction zone peridotites.

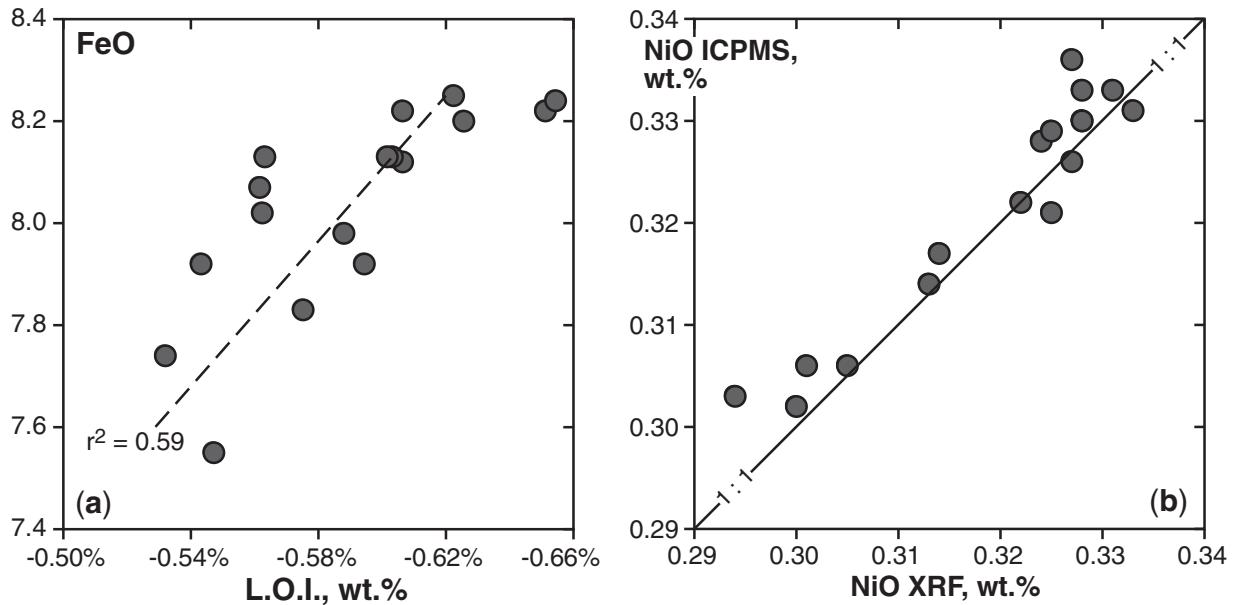


Fig. 10. (a) Loss on ignition (LOI, %) plotted vs total Fe as FeO in bulk-rocks. Negative LOI values indicate mass gain as a result of oxidation of FeO to Fe₂O₃ and demonstrate the near-absence of alteration in the Avacha peridotites. (b) Co-variation of NiO concentrations obtained by XRF and solution ICP-MS. The similarity of Ni contents from the two methods [together with the positive Fe–LOI trend in (a), which roughly corresponds to the rate of theoretical mass gain on ignition as a function of Fe content] testifies to the quality of the analytical data.

Avacha xenoliths in relation to continental and ocean island peridotites

Xenoliths from this study are compared in Fig. 11 with peridotites from the Horoman massif (Takazawa *et al.*, 2000), harzburgite xenoliths from ocean islands (Neumann *et al.*, 2002; Bonadiman *et al.*, 2005) and basalt-hosted xenoliths from central and SE Mongolia (Wiechert *et al.*, 1997; Ionov, 2007; Ionov & Hofmann, 2007). The majority of the Mongolian xenoliths were analysed in the same laboratory using the same procedures as the samples in this study. The Mongolian peridotites range from fertile to highly refractory and can be considered as broadly representative of the chemical variation range for intra-plate, off-craton lithospheric mantle. A set of analytical data of proven quality for type localities has been chosen for comparison with the Avacha data because larger literature compilations may contain inadequate data in terms of sample selection, preparation and accuracy, and hence 'blur' the evidence for mantle processes in co-variation plots as discussed by Ionov (2007) and Ionov & Hofmann (2007).

A major feature of the Avacha peridotites as a group is their very refractory character, with high MgO ($\geq 44\%$) and very low Al₂O₃ and CaO (0.4–0.9%), TiO₂ ($\leq 0.01\%$), Na₂O ($\leq 0.03\%$), K₂O and P₂O₅ (below detection limits). The Avacha xenoliths show fairly narrow chemical variation ranges and do not include more fertile or strongly metasomatized (with high Ca, Fe, alkalis) peridotites, which distinguishes them from nearly all

continental and ocean island peridotite suites. Another important difference is seen in the relations between Mg, Al and Si. The Avacha Mg–Al, Mg–Si and Al–Si trends cross those for intra-plate peridotites at $\sim 47\%$ MgO, $\sim 43.5\%$ SiO₂ and $\sim 0.5\%$ Al₂O₃ (Fig. 11a, c and d). As for the intra-plate peridotites, the contents of Al₂O₃ and SiO₂ in the Avacha xenoliths are negatively correlated with those of MgO, but the slopes of the linear correlation trends for the Avacha suite are distinct from those for peridotites from Mongolia and Horoman. Compared with the latter, the increase in Al₂O₃ in the Avacha suite as MgO decreases from 47 to 44% is smaller (Fig. 11a) but the increase in SiO₂ at lower MgO (Fig. 11b) and higher Al₂O₃ (Fig. 11d) is much stronger.

The range of FeO contents (7.55–8.25%, mainly 8.0–8.2%; see Fig. 11f) is fairly narrow. As discussed below, this may indicate the absence (or low degrees) of melt metasomatism and hence allow assessment of the depth of melt extraction (Ionov, 2007; Ionov & Hofmann, 2007). Another important observation in this regard is the absence of correlation between Mg# and Al₂O₃ (Fig. 11c). NiO is positively correlated with MgO but the slope of the correlation trend may be steeper than for the continental xenoliths (Fig. 11e).

Neumann & Simon (2009) have argued that ultra-refractory harzburgites sampled in subduction settings are chemically similar to harzburgite xenoliths from ocean islands. In detail, however, the data on Avacha peridotites in this study show significant differences from published

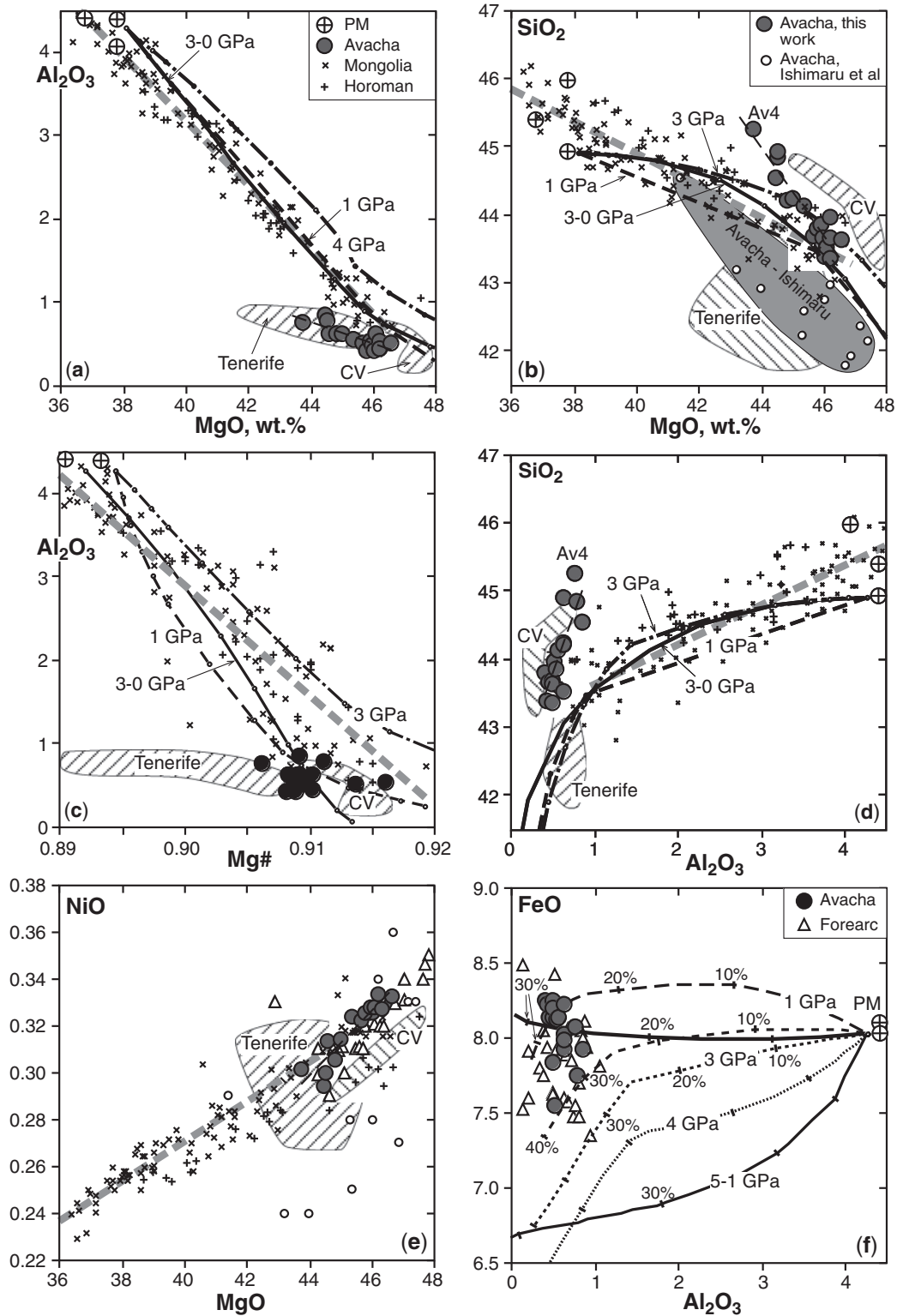


Fig. 11. Co-variation plots of major oxides (wt %) and Mg# in bulk-rock Avacha xenoliths in this study (filled circles) in comparison with those reported by Ishimaru *et al.* (2007) (small open circles) and in other refractory peridotite suites: off-craton intra-plate xenoliths from Mongolia (Wiechert *et al.*, 1997; Ionov, 2007; Ionov & Hofmann, 2007) (diagonal crosses), Horoman massif (Takazawa *et al.*, 2000) (crosses) and forearc peridotites (Parkinson & Pearce, 1998). Crossed circles are primitive mantle estimates (Hart & Zindler, 1986; McDonough & Sun, 1995; Palme & O'Neill, 2003). Bold dashed lines show melting residues of fertile spinel lherzolite at 1–4 GPa; bold continuous lines are residues of decompression melting at 3–0 GPa and 5–1 GPa (Herzberg, 2004). Linear correlation trends calculated for the Avacha peridotites in this study (fine dashed black lines) are distinct from the experimental melting trends and from the trends for continental xenoliths (bold grey dashed lines). The Avacha xenoliths plot off the melting residue trends in (a–d) and also differ in composition from published data on harzburgite xenoliths from the Tenerife and Cape Verde (CV) ocean islands (diagonal shaded fields) (Neumann *et al.*, 2002; Bonadiman *et al.*, 2005).

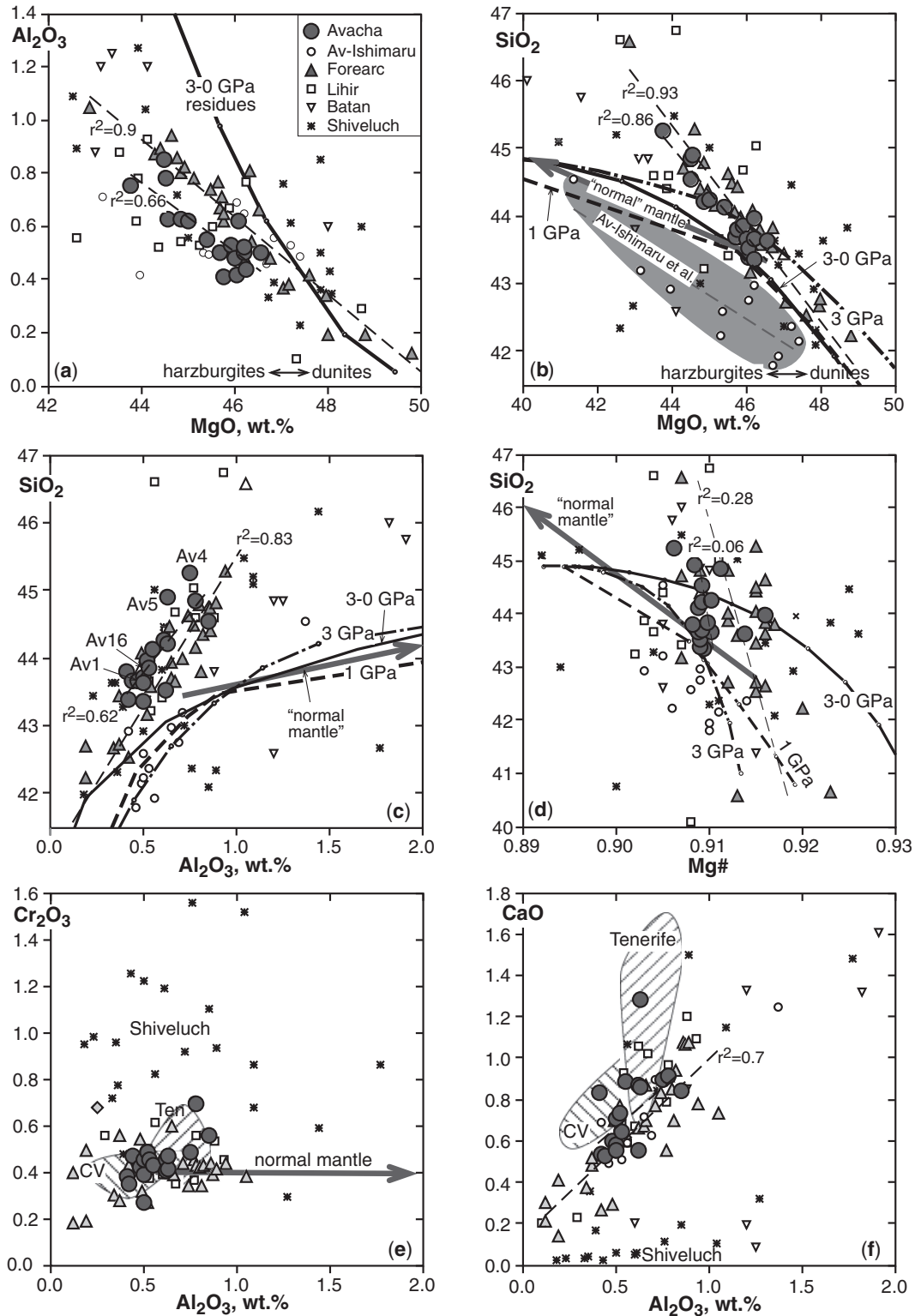


Fig. 12. Co-variations plots of major oxides (wt %) and Mg# in bulk-rock Avacha xenoliths from this study (filled circles), those reported by Ishimaru *et al.* (2007), serpentinized peridotites (recalculated to 100% anhydrous) from the Izu–Bonin–Mariana forearc (Parkinson & Pearce, 1998), and peridotite xenoliths from subduction-related volcanoes in the Western Pacific (Fig. 1a): Shiveluch (Bryant *et al.*, 2007), Batan (Maury *et al.*, 1992) and Lihir (McInnes *et al.*, 2001; Franz *et al.*, 2002). Fine dashed lines are linear correlation trends (r^2 values are correlation coefficients) for the Avacha and forearc peridotites. Bold arrows show correlation trends for ‘normal’ continental mantle (xenoliths from Mongolia). (See Fig. 11 for other symbols.)

data on ocean island harzburgites (Fig. 11). Those from Tenerife, for example, have much lower SiO_2 and Mg\# and also differ in their MgO-NiO relations. Harzburgites from Cape Verde plot off the trends defined by the Avacha xenoliths on the Mg-Al-Si diagrams. A major distinction is that the ocean island xenolith suites include abundant dunites, wehrlites, lherzolites and Fe-enriched rocks, which are absent in the Avacha suite.

Avacha xenoliths among other supra-subduction zone peridotites

Figures 11e, f and 12 compare Avacha xenoliths with peridotites of probably subduction-related provenance from the Western Pacific (Fig. 1a), including xenoliths from Batan (Maury *et al.*, 1992), Lihir (McInnes *et al.*, 2001; Franz *et al.*, 2002) and Shiveluch (Bryant *et al.*, 2007), and with serpentinites drilled on the ocean floor in the Bonin–Mariana forearc (Parkinson & Pearce, 1998). The plots and data presentation in this section focus, on the one hand, on elements such as Al, Cr, Ni and Mg that are considered to be relatively inert, providing robust melting indices, and on the other hand, on elements such as Si and Ca that may be mobile in a range of melts and fluids.

Whole-rock compositions are currently available for xenoliths from only two Kamchatka volcanoes, Avacha and Shiveluch. Chemical variation ranges for the Shiveluch peridotites are much wider and co-variation trends are more diffuse and may differ from those for the Avacha suite. Particularly important differences are seen in the Ca-Al-Cr relationships (Fig. 12e and f). The majority of the Shiveluch xenoliths are much lower in CaO ($\leq 0.2\%$) and higher in Cr_2O_3 ($\geq 0.7\%$); moreover, CaO and Cr_2O_3 abundances, unlike those for the Avacha suite, do not appear to be correlated with Al_2O_3 . This chemical evidence appears to corroborate the inference of Bryant *et al.* (2007), based on petrographic and other data, that the majority of the Shiveluch xenoliths are strongly metasomatized dunites; that is, are chemically and petrographically distinct from the Avacha harzburgites.

Whole-rock compositions are available for seven andesite-hosted xenoliths from Batan in the Philippines (Maury *et al.*, 1992) and 13 alkali basalt-hosted xenoliths dredged from the sea floor off Papua-New Guinea (Lihir: McInnes *et al.*, 2001; Franz *et al.*, 2002). Despite the small number of samples, the chemical variation ranges for peridotites at each locality match or exceed those for the larger Avacha suite in this study (Fig. 12). It is not clear to what extent the apparent chemical variations in both SE Pacific suites can be attributed to sample alteration and heterogeneity and quality of the analytical data. Most of the Batan xenoliths contain more Al, Ca, Na and K than the Avacha peridotites, consistent with evidence for modal metasomatism (Maury *et al.*, 1992). The Lihir xenoliths appear to be closer in chemistry to the Avacha suite and

define generally similar, but more diffuse, oxide co-variation trends.

Despite the very high LOI (7–24%) in the serpentinized peridotites from the Izu–Bonin–Mariana (IBM) forearc (Parkinson & Pearce, 1998), their volatile-free compositions recalculated to 100% show remarkable similarities to those of the Avacha suite, except that the IBM suite also contains MgO -rich (47–50%) dunites. Oxide co-variation trends in the Izu–Bonin–Mariana and Avacha suites have nearly identical slopes, with very similar contents of SiO_2 , Al_2O_3 , Cr_2O_3 , CaO and NiO at a given MgO % (Fig. 11e and 12). The range of FeO in the two suites are nearly the same; however, the forearc rocks tend to have lower FeO and higher Mg\# (Figs 11f and 12d). Relatively high Na_2O (0.02–0.28%) and K_2O (0.01–0.04%) in the forearc rocks are not likely to be a primary feature and appear to be related to serpentinization.

To sum up, the close similarities between the Avacha and the Izu–Bonin–Mariana forearc peridotites appear to indicate that these two geographically distant suites sample similar refractory lithospheric mantle reservoirs, which may be dominant in the shallow mantle wedge. The Lihir xenoliths appear to originate from the same reservoir but may have been affected by late-stage processes, such as interaction with alkali magmas and hydrothermal fluids. Xenoliths from Batan and Shiveluch may reflect lithospheric heterogeneities in the vicinity of active arc volcanoes as a result of reaction of the lithosphere with large volumes of melt.

Relations between bulk-rock and mineral compositions and temperature estimates

Relations between bulk-rock and mineral compositions are illustrated in Fig. 13a–d. Figure 13a compares Mg\# in whole-rocks (WR), olivine and opx. In each sample, $\text{Mg\#}_{\text{Opx}} > \text{Mg\#}_{\text{Ol}} > \text{Mg\#}_{\text{WR}}$. The fact that Mg\# both in olivine and opx, which together make up >95% of the xenoliths, are higher than Mg\#_{WR} is explained by the very low Mg\# in the coexisting spinel (0.55–0.64; Table 3) as shown previously for other peridotite xenolith suites (Ionov *et al.*, 2005c; Ionov, 2007). Mg\#_{WR} values calculated based on the Mg\# and modal abundances of olivine, opx and spinel reproduce the measured Mg\# values within ± 0.001 . Although it is common and mostly sensible to use Mg\#_{Ol} as a proxy for Mg\#_{WR} in mantle peridotites (e.g. Mg\#_{Ol} and Mg\#_{WR} in the Avacha suite show linear correlation with correlation coefficient $r^2 = 0.95$), one should keep in mind the minor differences between Mg\#_{Ol} and Mg\#_{WR} .

Mg\#_{Ol} in the Avacha peridotites is not correlated with whole-rock Al_2O_3 (Fig. 13d) or CaO , consistent with the absence of correlations between Mg\# and Al_2O_3 (or CaO) in the whole-rocks (Fig. 11c). Cr\#_{Sp1} shows a weak ($r^2 = 0.21$) negative correlation with whole-rock Al_2O_3

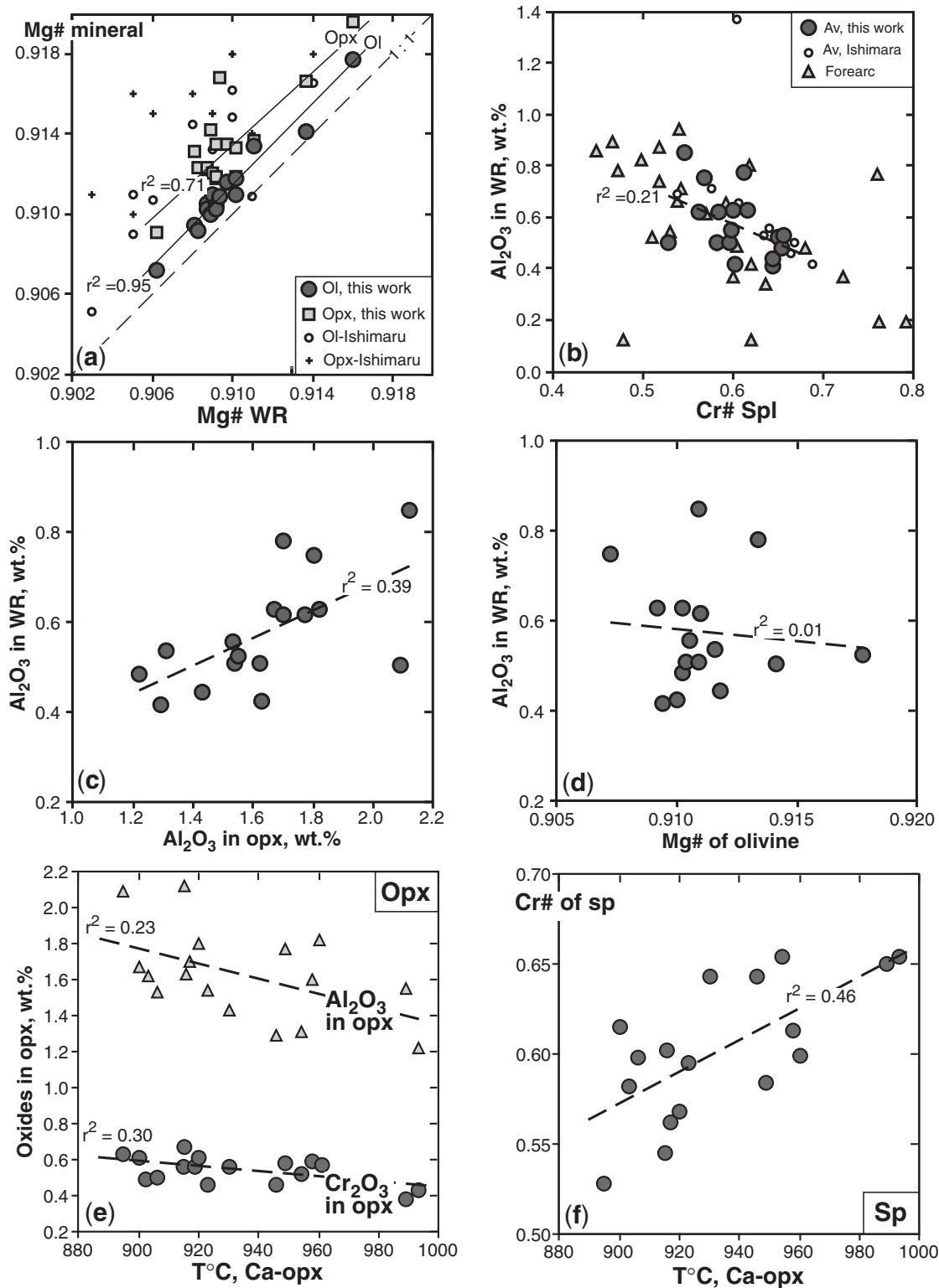


Fig. 13. Co-variation plots for mineral and bulk-rock compositions and temperature (T) estimates (Brey & Köhler, 1990) in Avacha xenoliths from this study (ES Table 1). Also shown in (a, b) are data for Avacha xenoliths from Ishimaru *et al.* (2007) and for forearc peridotites (Parkinson & Pearce, 1998); straight lines are linear correlation trends for data from this study, r^2 values are correlation coefficients. (a) A plot of $Mg\#_{WR}$ vs $Mg\#_{Ol}$ and $Mg\#_{Opx}$ from this study defines clear trends parallel to the line of equal $Mg\#$ (dashed diagonal line, 1:1); data from the earlier studies show more scatter and are systematically higher. (b, c) Whole-rock (WR) Al_2O_3 is negatively correlated with $Cr\#_{Sp}$ (b) and positively correlated with Al_2O_3 in opx (c) consistent with an origin of the Avacha (and forearc) peridotites as melting residues. (d) $Mg\#_{Ol}$ shows no correlation with bulk-rock Al_2O_3 , possibly as a result of pressure effects on FeO in melting residues (see Fig. 11f). (e, f) Spinel and opx compositions are related to their equilibration T , with higher $Cr\#_{sp}$ and lower Al and Cr in opx at higher T . Temperature effects on $Cr\#_{sp}$ (i.e. changes in spinel composition on cooling) may explain the low correlation coefficient for the trend in (b).

(Fig. 13b) and a more robust ($r^2=0.46$) positive correlation with equilibration temperatures (Fig. 13f). The latter $\text{Cr}\#_{\text{Spl}}-T$ correlation is unusual for refractory mantle peridotites. It cannot be due to increasing degrees of melt extraction with depth (assuming that higher T s indicate greater depths) because whole-rock Al_2O_3 is not correlated with temperature. It appears that $\text{Cr}\#_{\text{Spl}}$ can evolve on cooling as a result of temperature-controlled redistribution of Cr and Al between spinel, opx and cpx and changes in their modal abundances. In such a case, $\text{Cr}\#_{\text{Spl}}$ could be affected both by melting degree and post-melting chemical inter-mineral re-equilibration; the effects of cooling over a wide T range should be apparent for peridotite suites with narrow ranges of melt extraction, such as those from Avacha. The contents of Al_2O_3 in opx are correlated both with whole-rock Al_2O_3 (Fig. 13c) and with temperature (Fig. 13e) possibly showing the combined effects of melting degree and cooling, as for $\text{Cr}\#_{\text{Spl}}$.

Modal olivine is negatively correlated with whole-rock Al_2O_3 , Cr_2O_3 and CaO (Fig. 14a). Because olivine and opx abundances in the harzburgites are complementary, this implies that whole-rock Al_2O_3 , Cr_2O_3 and CaO are positively correlated with modal opx. The contents of Al_2O_3 in bulk-rocks and opx are also positively correlated (Fig. 13c). Modal olivine shows a very weak ($r^2=0.1$) positive correlation with $\text{Mg}\#_{\text{Ol}}$. To sum up, some of the parameters presented in this section ($\text{Mg}\#_{\text{WR}}$, $\text{Mg}\#_{\text{Ol}}$, $\text{Cr}\#_{\text{Spl}}$, whole-rock Al_2O_3 , modal olivine) are correlated to each other (whole-rock Al_2O_3 vs modal olivine and $\text{Cr}\#_{\text{Spl}}$) whereas others are not, even though they are commonly viewed as more or less robust melt extraction indices.

A distinctive petrological feature of the Avacha peridotites is a combination of very low modal cpx (1.5–3%) and variable but generally high modal opx (18–30%); this results in high opx/ol and low cpx/opx and cpx/ol ratios. A plot of modal olivine vs opx and cpx (Fig. 14d) shows that at a given olivine content the Avacha harzburgites have higher modal opx than refractory peridotite xenoliths in continental intra-plate basalts and that this opx ‘surplus’ increases from 2–3% at 76–79% olivine to 5–10% at 67–70% olivine. In other words, as modal opx in the Avacha suite increases from 18 to 30%, modal cpx remains nearly the same; as a result, all the Avacha xenoliths (67–80% olivine) are harzburgites, whereas intra-plate spinel peridotites with <75% olivine are usually lherzolites (>5% cpx, Fig. 14d). Thus, the high modal opx in the Avacha harzburgites is balanced by low modal cpx (the sum of ol + opx + cpx in the peridotites is ~98%, the remainder being spinel and amphibole).

In terms of whole-rock chemistry, the higher modal opx and lower cpx at a given modal per cent olivine in the Avacha harzburgites is expressed as higher WR silica (Fig. 11b) and lower CaO at a given MgO or Al_2O_3 .

Moreover, the contents of Al_2O_3 and CaO in the Avacha peridotites are generally much lower at given modal per cent olivine than in the intra-plate peridotites (Fig. 14b).

Trace element compositions

Trace element compositions of 17 bulk-rock Avacha peridotites are listed in Table 4. Ni abundances obtained by solution ICP-MS and by XRF (Table 2) are very similar to each other (Fig. 10b) testifying to the data quality. LA-ICP-MS analyses of opx and olivine are listed in Table 5. Table 3 of the ES provides the complete set of trace element analyses from this study, including those of the reference materials. Primitive mantle-normalized REE and trace element patterns are shown in Fig. 15 for representative bulk-rocks and in Fig. 16 for olivine and opx. Bulk-rock abundances are plotted in Fig. 17 vs Al_2O_3 and other melt extraction indices. Figure 18 shows plots of La vs Sr and Ba, U/Th and Nb/Ta and modal amphibole.

The REE patterns of bulk-rocks and opx show continuously decreasing normalized abundances from Lu to Ho or Eu and nearly flat middle to light REE (MREE–LREE) patterns. The very low heavy REE (HREE) abundances in the Avacha xenoliths (0.05–0.1 of those in primitive mantle) can be modelled by $\geq 20\%$ of incremental melting of a fertile spinel lherzolite (Ionov, 2004, and references therein) or higher melting degrees for ‘open-system’ melting (Godard *et al.*, 2008). Flat MREE–LREE patterns in refractory peridotites could be due to retention of melt in the residue or, more probably, to post-melting metasomatism (see below). Extended trace element patterns of the Avacha peridotites show spikes at Sr, Pb, U, Rb and Ba. It is tempting to relate the positive anomalies of these fluid-mobile elements to metasomatism by subduction-related fluids; however, very similar trace element patterns and abundances have also been reported from ultra-refractory abyssal peridotites (Godard *et al.*, 2008).

The abundances and ratios of some moderately incompatible trace elements in the Avacha xenoliths show linear correlations with a number of melt extraction indices (Fig. 17), indicating that their behaviour is mainly controlled by partial melting. The correlation coefficients for the HREE decrease from Lu to Er; that is, with decreasing compatibility. Furthermore, the correlation coefficients for Lu and Yb are the highest in plots vs bulk-rock Al_2O_3 and are consistently lower on plots vs modal olivine, $\text{Cr}\#_{\text{Sp}}$ and $\text{Mg}\#_{\text{WR}}$ respectively. The last plot shows no statistically meaningful HREE– $\text{Mg}\#_{\text{WR}}$ correlations. Thus, the trace element data confirm that bulk-rock Al_2O_3 and modal olivine are the most robust melt extraction indices for the Avacha suite, whereas $\text{Mg}\#_{\text{WR}}$ does not appear to be explicitly related to the melting degree. Surprisingly, Rb and Nb are also positively correlated with Al_2O_3 .

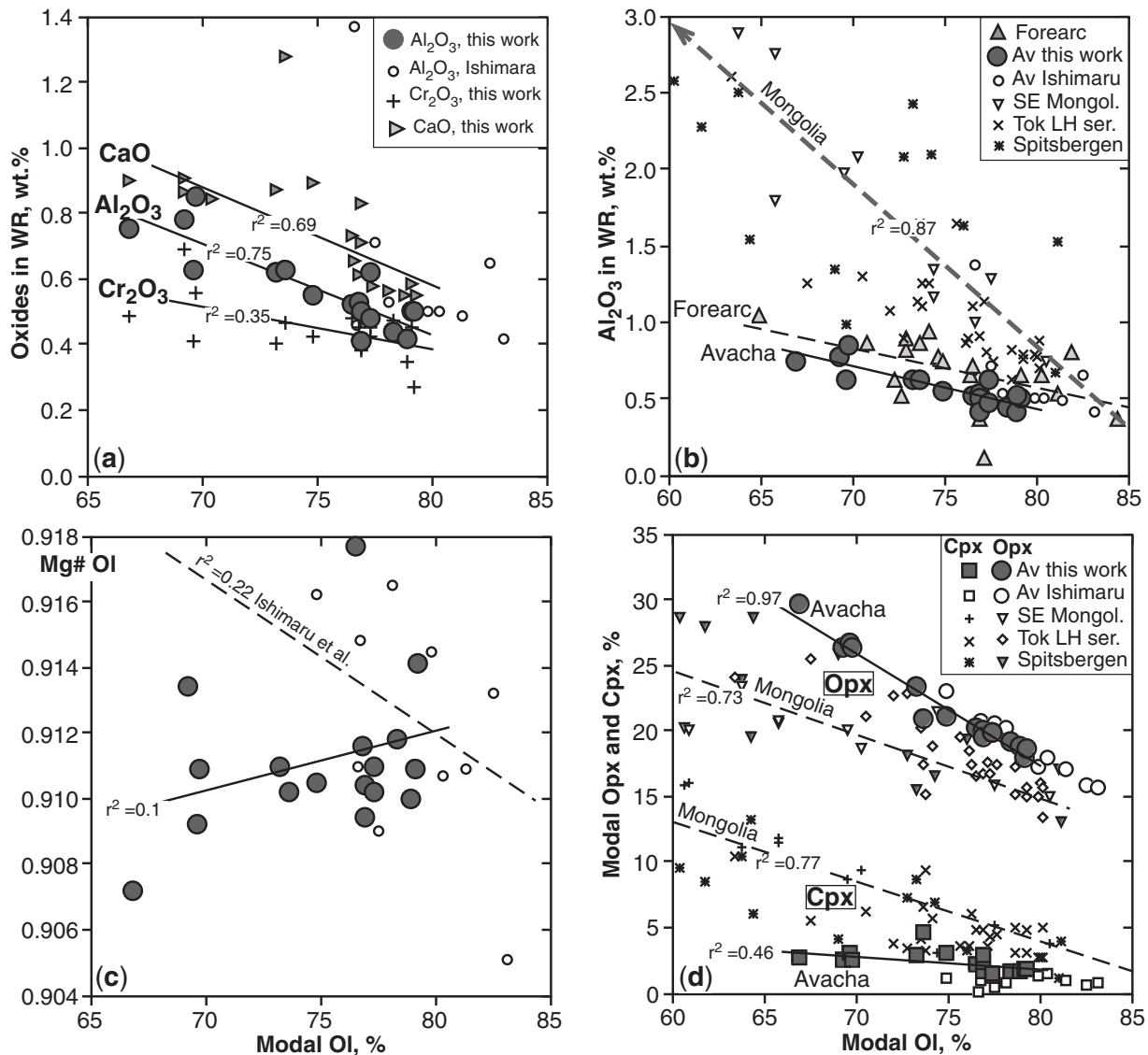


Fig. 14. Modal olivine contents in Avacha peridotites plotted vs selected oxides in bulk-rocks (a, b), Mg# of olivine (c) and modal opx and cpx (d). Also shown in (b) and (d) are data for basalt-hosted xenoliths from SE Mongolia (Wiechert *et al.*, 1997), SE Siberia (Ionov *et al.*, 2005c) and Spitsbergen (Ionov *et al.*, 2002, and unpublished data of the author) obtained in the same laboratory, and for forearc peridotites (Parkinson & Pearce, 1998). Linear correlation trends are shown as fine continuous lines for the Avacha peridotites and dashed lines for the other suites; r^2 values are correlation coefficients. The contents of Al₂O₃ and modal cpx are lower in the Avacha peridotites than in the continental intra-plate peridotite xenoliths at similar modal olivine, whereas modal opx is higher.

(Fig. 17a), but show poor correlations with other highly incompatible elements.

La abundances (as well as those of all LREE and MREE) show robust positive correlations with the proportion of modal amphibole (Fig. 18a) and Sr and Ba contents (Fig. 18b), thus clearly establishing links between these highly incompatible elements and modal metasomatism. The U/Th and Nb/Ta ratios are low in those xenoliths with higher La (and amphibole) and high in low-La xenoliths (Fig. 18c and d).

THE ORIGIN OF SUPRA-SUBDUCTION LITHOSPHERIC MANTLE

The petrological and chemical data on the Avacha peridotites presented above characterize a section of the shallow mantle wedge lithosphere ‘sampled’ by the xenoliths. These results are discussed below to better constrain the origin of the mantle beneath Avacha, in the Western Pacific and in other subduction zones. This discussion

Table 4: Trace element abundances in Avacha peridotites determined by solution ICP-MS (in ppm except for NiO in wt %)

	Av1	Av2	Av3	Av4	Av5	Av6	Av7	Av8	Av9	Av10	Av11	Av12	Av13	Av14	Av15	Av16	Av17
NiO %	0.322	0.328	0.329	0.306	0.314	0.333	0.336	0.302	0.330	0.317	0.326	0.330	0.321	0.303	0.306	0.331	0.333
Ti	5.8	6.3	7.8	11.4	9.9	17.4	8.8	9.6	8.8	8.6	9.3	12.0	23.8	13.2	11.4	9.2	13.1
V	36	38	39	51	43	36	33	53	40	40	34	39	27	45	42	35	27
Co	132	131	133	127	125	135	135	124	139	127	131	135	135	126	126	133	131
Cu	6.2	1.9	6.6	2.0	3.0	2.3	2.0	2.6	4.6	5.6	2.1	2.7	2.0	4.0	2.4	2.8	6.7
Zn	39	42	46	46	46	45	46	47	43	40	41	56	37	46	51	40	44
Rb	0.11	0.10	0.08	0.11	0.12	0.11	0.07	0.16	0.11	0.10	0.10	0.10	0.05	0.13	0.09	0.10	0.06
Sr	0.79	0.32	0.28	0.126	1.57	1.96	0.164	1.67	0.55	0.62	0.160	1.57	2.11	1.17	1.16	0.73	0.23
Y	0.229	0.045	0.065	0.058	0.075	0.096	0.027	0.065	0.075	0.054	0.046	0.070	0.134	0.119	0.076	0.070	0.095
Zr	0.151	0.104	0.102	0.073	0.205	0.420	0.109	0.363	0.093	0.126	0.098	0.219	0.427	0.250	0.208	0.093	0.098
Nb	0.011	0.012	0.009	0.011	0.011	0.014	0.009	0.027	0.010	0.009	0.010	0.012	0.008	0.018	0.012	0.013	0.007
Cs	0.002	0.001	0.001	0.000	0.003	0.002	0.001	0.002	0.001	0.002	0.001	0.001	0.002	0.001	0.001	0.001	0.001
Ba	0.56	0.27	0.28	0.19	0.88	0.75	0.17	1.14	0.39	0.39	0.26	0.45	0.85	0.71	0.24	0.17	0.34
La	0.0226	0.0057	0.0101	0.0050	0.0120	0.0233	0.0026	0.0392	0.0110	0.0051	0.0040	0.0148	0.0240	0.0193	0.0116	0.0119	0.0058
Ce	0.108	0.014	0.025	0.014	0.032	0.060	0.007	0.063	0.034	0.013	0.010	0.039	0.068	0.056	0.031	0.032	0.014
Pr	0.024	0.0022	0.0041	0.0018	0.0047	0.0088	0.0010	0.0066	0.0059	0.0020	0.0016	0.0062	0.0110	0.0089	0.0040	0.0051	0.0027
Nd	0.130	0.009	0.018	0.008	0.023	0.040	0.005	0.024	0.029	0.009	0.007	0.028	0.053	0.041	0.017	0.024	0.015
Sm	0.047	0.0030	0.0056	0.0027	0.0067	0.0108	0.0019	0.0066	0.0074	0.0031	0.0030	0.0080	0.0147	0.0130	0.0048	0.0082	0.0050
Eu	0.0095	0.0007	0.0013	0.0006	0.0022	0.0040	0.0004	0.0021	0.0018	0.0008	0.0007	0.0028	0.0056	0.0040	0.0016	0.0024	0.0014
Gd	0.048	0.0030	0.0059	0.0029	0.0072	0.0112	0.0015	0.0064	0.0093	0.0029	0.0032	0.0080	0.0157	0.0120	0.0045	0.0084	0.0060
Tb	0.0095	0.0005	0.0012	0.0007	0.0013	0.0019	0.0003	0.0012	0.0015	0.0007	0.0006	0.0015	0.0028	0.0026	0.0011	0.0016	0.0012
Dy	0.058	0.0047	0.0093	0.0065	0.0095	0.0129	0.0030	0.0087	0.0098	0.0061	0.0054	0.0105	0.0189	0.0199	0.0088	0.0106	0.0099
Ho	0.0111	0.0015	0.0024	0.0021	0.0024	0.0030	0.0009	0.0024	0.0023	0.0018	0.0014	0.0024	0.0043	0.0049	0.0026	0.0026	0.0027
Er	0.031	0.0070	0.0093	0.0101	0.0098	0.0114	0.0046	0.0099	0.0081	0.0081	0.0062	0.0094	0.0150	0.0182	0.0109	0.0091	0.0111
Tm	0.0047	0.0018	0.0021	0.0025	0.0022	0.0021	0.0013	0.0023	0.0017	0.0020	0.0014	0.0019	0.0026	0.0036	0.0025	0.0019	0.0024
Yb	0.033	0.018	0.018	0.025	0.021	0.019	0.014	0.022	0.016	0.020	0.014	0.019	0.022	0.033	0.023	0.017	0.023
Lu	0.0062	0.0040	0.0040	0.0053	0.0046	0.0041	0.0034	0.0048	0.0035	0.0044	0.0033	0.0042	0.0045	0.0064	0.0048	0.0037	0.0047
Hf	0.0032	0.0019	0.0029	0.0013	0.0042	0.0089	0.0022	0.0044	0.0016	0.0025	0.0021	0.0048	0.0096	0.0040	0.0038	0.0013	0.0020
Ta	0.0007	0.0002	0.0002	0.0001	0.0002	0.0005	0.0021	0.0015	0.0007	0.0010	0.0002	0.0014	0.0008	0.0010	0.0008	0.0012	0.0003
Pb	0.021	0.013	0.025	0.015	0.034	0.015	0.031	0.035	0.021	0.013	0.019	0.020	0.017	0.020	0.013	0.021	0.331
Th	0.0033	0.0019	0.0007	0.0005	0.0012	0.0035	0.0003	0.0136	0.0008	0.0007	0.0004	0.0015	0.0036	0.0028	0.0014	0.0005	0.0005
U	0.0014	0.0057	0.0003	0.0004	0.0009	0.0016	0.0003	0.0046	0.0006	0.0003	0.0005	0.0010	0.0028	0.0018	0.0007	0.0011	0.0004

primarily seeks to explore relations between (1) partial melting, (2) interaction of the melting residues with subduction-related fluids (metasomatism) in the mantle wedge, and (3) late-stage modifications related to recent tectonic and magmatic activity.

Textural, thermal and mineralogical evolution

Calculated equilibration temperatures range from 900 to 1000°C, and possibly were even lower (800–900°C), in the protolith of the Avacha xenoliths shortly before their entrapment in the host magma. The xenolith suite shows clear evidence (unmixing and core–rim zoning of coarse

opx, interstitial cpx) for long-term cooling and may also record recent local, small-scale heating related to precipitation of fine-grained materials. As for other highly refractory mantle peridotites worldwide (e.g. Simon *et al.*, 2003; Pearson & Wittig, 2008; Simon *et al.*, 2008), the cpx in the Avacha peridotites is not likely to be a residual phase after partial melting, but is rather related to unmixing from high- T , (Ca,Al)-rich residual opx.

Taken together, the T estimates and petrographic observations indicate three main stages in the evolution of the Avacha peridotites. (1) They were initially produced as residues after high degrees of melt extraction, which consisted of olivine, (Ca,Al)-rich opx \pm accessory Cr-spinel. (2)

Table 5: Element abundances in orthopyroxene and olivine determined by LA-ICP-MS, in ppm (except for CaO, wt %)

	Av1	Av2	Av3	Av4	Av5	Av6	Av7	Av8	Av9	Av10	Av11	Av12	Av13	Av14	Av15	Av16	Av17
<i>Orthopyroxene</i>																	
CaO av.	0.41	0.69	0.58	0.84	0.57	0.89	0.64	0.70	0.57	0.73	0.57	0.82	0.88	0.57	1.07	0.66	0.58
CaO min.	0.27	0.48	0.52	0.45	0.53	0.83	0.41	0.45	0.47	0.56	0.42	0.56	0.70	0.48	0.66	0.46	0.40
Ti	27	30	32	42	30	38	42	29	24	34	46	31	30	43	31	28	65
V	101	100	100	105	96	90	97	104	93	104	90	114	94	98	99	75	96
Co	59	56	54	56	57	53	53	51	55	54	55	53	53	53	53	57	52
Ni	694	610	569	600	643	556	555	533	610	593	621	592	571	584	573	674	558
Sr	0.030	0.004	0.013	0.002	0.099	0.086	0.005	0.198	0.063	0.010	0.025	0.005	0.041	0.022	0.005	0.083	0.010
Y	0.073	0.079	0.098	0.091	0.059	0.105	0.051	0.074	0.061	0.087	0.086	0.071	0.091	0.098	0.103	0.051	0.106
Zr	0.005	0.004	0.010	0.003	0.004	0.134	0.004	0.013	0.226	0.004	0.085	0.006	0.062	0.006	0.004	0.063	0.015
Nb	0.006	0.003	0.003	0.004	0.004	0.003	0.003	0.003	0.003	0.004	0.004	0.004	0.004	0.004	0.004	0.004	0.004
Ba	0.036	0.033	0.037	0.009	0.064	0.004	0.005	0.264	0.059	0.010	0.124	0.001	0.014	0.030	0.003	0.077	0.086
La	0.0022	0.0011	0.0011	0.0001	0.0010	0.0017	0.0004	0.0050	0.0048	0.0003	0.0009	0.0005	0.0008	0.0009	0.0003	0.005	0.0005
Ce	0.0088	0.0047	0.0034	b.d.	0.0038	0.0042	0.0017	0.0043	0.0152	0.0008	0.0035	0.0013	0.0025	0.0030	0.0009	0.014	0.0010
Pr	0.0025	0.0009	0.0007	0.0000	0.0003	0.0005	0.0004	0.0007	0.0024	0.0002	0.0005	0.0002	0.0002	0.0006	0.0001	0.002	0.0002
Nd	0.0137	0.0047	0.0035	0.0002	0.0030	0.0024	0.0014	0.0023	0.0120	0.0006	0.0040	0.0009	0.0026	0.0032	0.0005	0.012	0.0013
Sm	0.0057	0.0014	0.0021	0.0001	0.0014	0.0011	b.d.	0.0007	0.0027	b.d.	0.0016	0.0006	0.0010	0.0009	0.0004	0.001	0.0001
Eu	0.0010	0.0002	0.0005	0.0000	0.0004	0.0005	0.0002	0.0004	0.0010	b.d.	0.0003	b.d.	0.0004	0.0003	b.d.	0.001	0.0001
Gd	0.0056	0.0012	0.0032	0.0002	0.0011	0.0019	0.0007	0.0010	0.0041	0.0003	0.0025	0.0003	0.0016	0.0018	0.0007	0.004	0.0014
Tb	0.0017	0.0003	0.0006	0.0002	0.0003	0.0007	0.0002	0.0003	0.0009	0.0002	0.0007	0.0002	0.0005	0.0006	0.0003	0.001	0.0004
Dy	0.014	0.005	0.009	0.005	0.004	0.008	0.003	0.005	0.005	0.006	0.006	0.004	0.008	0.008	0.007	0.006	0.008
Ho	0.0030	0.0028	0.0033	0.0029	0.0020	0.0034	0.0016	0.0024	0.0020	0.0026	0.0027	0.0021	0.0028	0.0032	0.0036	0.0021	0.0032
Er	0.015	0.017	0.018	0.019	0.014	0.020	0.013	0.017	0.011	0.019	0.016	0.018	0.015	0.022	0.023	0.011	0.022
Tm	0.004	0.005	0.005	0.006	0.004	0.005	0.004	0.005	0.003	0.006	0.005	0.006	0.005	0.006	0.006	0.003	0.006
Yb	0.049	0.059	0.059	0.061	0.046	0.057	0.052	0.058	0.044	0.065	0.047	0.067	0.053	0.073	0.063	0.035	0.074
Lu	0.011	0.014	0.014	0.015	0.012	0.013	0.013	0.013	0.010	0.015	0.012	0.016	0.013	0.017	0.015	0.009	0.017
Pb	0.034	0.020	0.024	0.021	0.022	0.023	0.014	0.019	0.027	0.016	0.018	0.027	0.035	0.017	0.016	0.014	0.013
Th	0.00032	0.00002	0.00012	0.00001	0.00035	0.00043	0.00005	0.0026	0.0053	0.00043	0.00098	0.00005	0.00019	0.00021	0.00004	0.0006	0.00013
U	0.00038	0.00042	0.00008	0.00015	0.00009	0.00087	0.00013	0.0029	0.0017	0.00003	0.00062	0.00002	0.00019	0.00028	0.00002	0.0011	0.00002
<i>Olivine</i>																	
Al	19	17	19	13	19	26	16	23	20	16	15	27	22	23	18	31	15
Ti	1.1	1.6	1.8	1.9	1.6	1.5	1.8	1.5	1.4	1.8	1.6	1.6	1.3	1.7	1.5	1.7	2.4
V	1.9	1.8	2.0	1.0	2.2	1.8	1.7	2.1	1.8	2.3	1.8	2.1	1.8	1.4	1.4	2.1	1.2
Cr	17	30	19	19	33	60	20	44	21	35	21	42	62	20	16	49	26
Co	131	136	135	139	137	136	137	134	132	136	136	135	134	133	135	130	132
Y	0.002	0.001	0.002	0.001	0.002	0.003	0.001	0.002	0.001	0.002	0.002	0.002	0.003	0.002	0.001	0.002	0.001
Yb	0.0035	0.0022	0.0024	0.0017	0.0023	0.0037	0.0015	0.0020	0.0018	0.0027	0.0017	0.0021	0.0022	0.0024	0.0019	0.0035	0.0031
Lu	0.0011	0.0009	0.0009	0.0007	0.0009	0.0010	0.0010	0.0008	0.0007	0.0010	0.0007	0.0009	0.0007	0.0011	0.0009	0.0010	0.0012

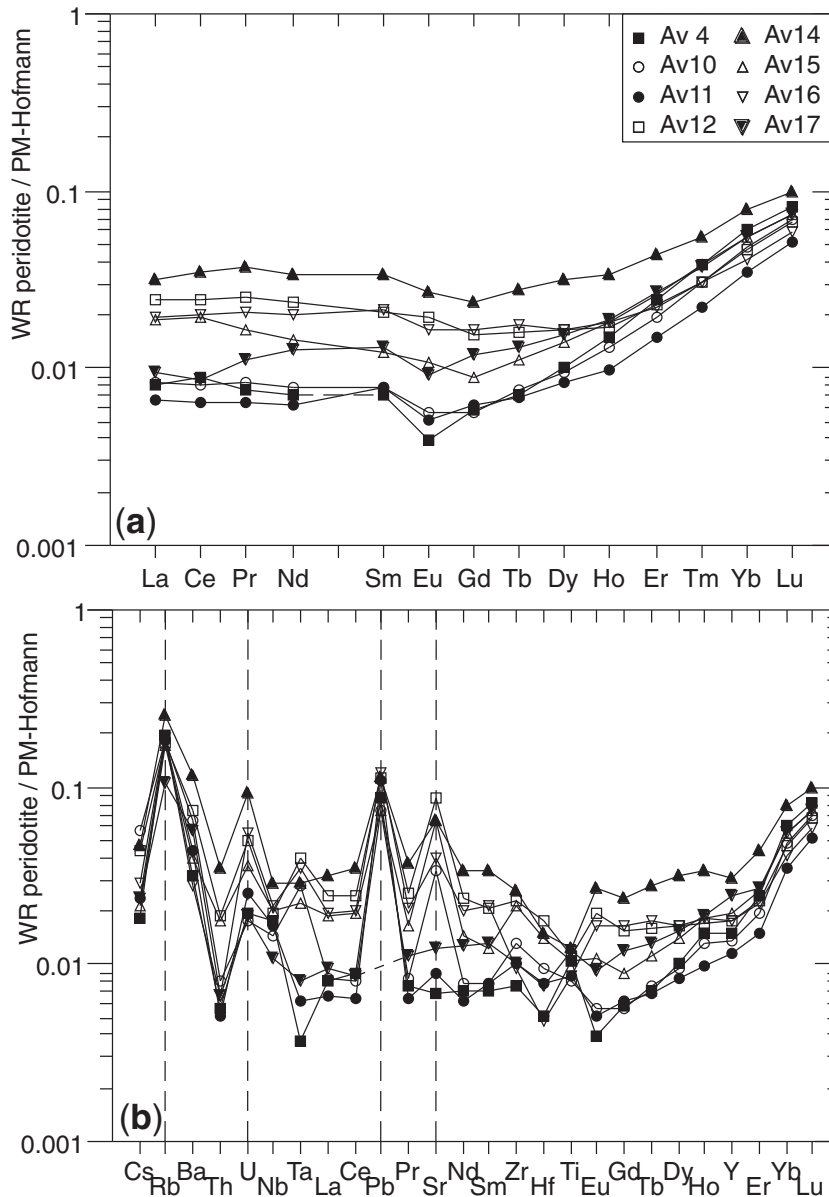


Fig. 15. Primitive mantle-normalized (Hofmann, 1988) REE patterns (a) and multi-element patterns (b) in representative bulk-rock Avacha peridotites.

Slow cooling from sub-magmatic temperatures resulted in unmixing of the high- T opx to form cpx and spinel lamellae in opx cores and precipitation of interstitial cpx, and affected mineral compositions. (3) Tectonic activity shortly before the transport of the xenoliths to the surface induced fracturing and local re-crystallization. Infiltration of hydrous fluids, probably facilitated by the fracturing, resulted in the precipitation of accessory amphibole and possibly some additional cpx, and may have been accompanied by localized, short-term rises in temperature.

These inferences imply a long period of time between the last partial melting event and recent re-crystallization

and metasomatism. The latter processes are more likely to be related to local phenomena in the vicinity of the magma conduits that fed the host lavas rather than direct transport of fluids produced by slab dehydration (through ~ 80 km of the mantle wedge and the partial melting zone responsible for the magmatic activity) to the lithosphere.

The role and conditions of partial melting

Partial melting conditions can be constrained using co-variation plots of modal abundances and major elements, such as Al and Mg, that are considered to be relatively inert in post-melting processes, in comparison with

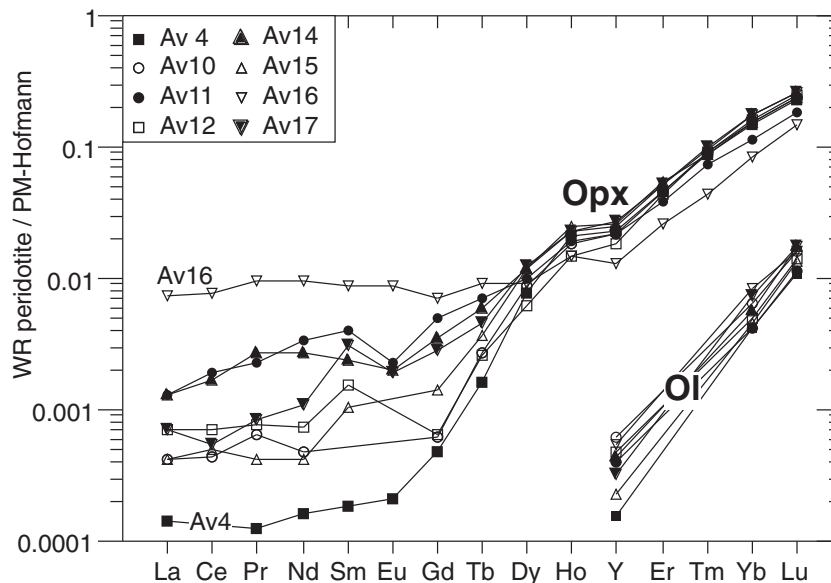


Fig. 16. Primitive mantle-normalized (Hofmann, 1988) REE and Y patterns in coarse opx and olivine.

experimental melting trends. Particular difficulties for subduction zone mantle are the poorly constrained source materials, complex dynamic processes and probably involvement of various amounts of fluid that either trigger the melting (Grove *et al.*, 2006) or metasomatize the residues soon after their formation.

A number of petrological parameters (modal olivine and opx, whole-rock Al_2O_3 and MgO, $Cr\#_{Spl}$, $Mg\#_{Ol}$, $Mg\#_{WR}$) are commonly viewed as more or less robust melt extraction indices. Whereas some of these parameters, reported here for the Avacha peridotites, show correlations consistent with an origin as melting residues (in particular, whole-rock Al_2O_3 and modal olivine), others do not. The latter in particular concerns the lack of correlation of $Mg\#_{Ol}$ (or $Mg\#_{WR}$) with the other indices and the relatively poor correlations involving $Cr\#_{Spl}$. These features should not be considered as evidence contradicting an origin of the Avacha suite initially as melt extraction residues, but rather to reflect a complex, possibly multi-stage, melting and post-melting history. As shown above, the $Cr\#_{Spl}$ is temperature-dependent and was probably affected by re-equilibration on cooling. As discussed below, $Mg\#$ is sensitive to the depth of partial melting (Herzberg, 2004; Ionov & Hofmann, 2007) and can also be affected by late-stage residue–melt interactions and percolation of mafic melts (Kelemen, 1990; Bodinier & Godard, 2003; Ionov, 2007). Overall, the petrological and trace element data indicate that bulk-rock Al_2O_3 and modal olivine are the most robust melt extraction indices for the Avacha suite.

The absence of primary cpx together with the high $Mg\#_{Ol}$ and $Cr\#_{Sp}$ in the Avacha suite require high

melting degrees and temperatures and/or fluid fluxing during melting. The melting degrees obtained from comparisons of the whole-rock Al and Mg contents in the Avacha peridotites with experimental data (Walter, 2003; Herzberg, 2004) (Fig. 11a and f) range from ~28 to 35%. Because Fe contents in residual peridotites are sensitive to the depth of melting, and assuming no post-melting Fe enrichment, the Al–Fe relations (Fig. 11f) indicate that melting took place at ≤ 1 GPa to 2 GPa (Herzberg, 2004). The relatively shallow melt extraction depth (<65 km) could be consistent with melting either at a mid-ocean ridge or in the mantle wedge. The former, however, is not very likely because of the consistently refractory nature and narrow chemical variation range of the Avacha suite in contrast to the wide compositional variations in abyssal peridotites, believed to be representative of residues formed at mid-ocean ridges (e.g. Bodinier & Godard, 2003; Niu, 2004; Godard *et al.*, 2008; Simon *et al.*, 2008). Thus, the Avacha suite was probably produced by ‘hydrous’ melting in the shallow mantle wedge (e.g. Hirose & Kawamoto, 1995; Hirschmann *et al.*, 1998; Grove *et al.*, 2006).

Further support for this inference comes from the fact that some oxide and modal co-variation trends in the Avacha suite (Mg–Al, Mg–Si, Al–Si, $Mg\#$ –Al, olivine–Al; Figs 11, 12 and 14) differ significantly from those both in ‘dry’ melting experiments and in intra-plate peridotite series believed to be ‘dry’ melting residues as discussed above. In comparison, it is possible that the chemical and modal variations in the Avacha suite could be explained by differences in either depth or water content during high-degree fluid-fluxed melting, although this hypothesis

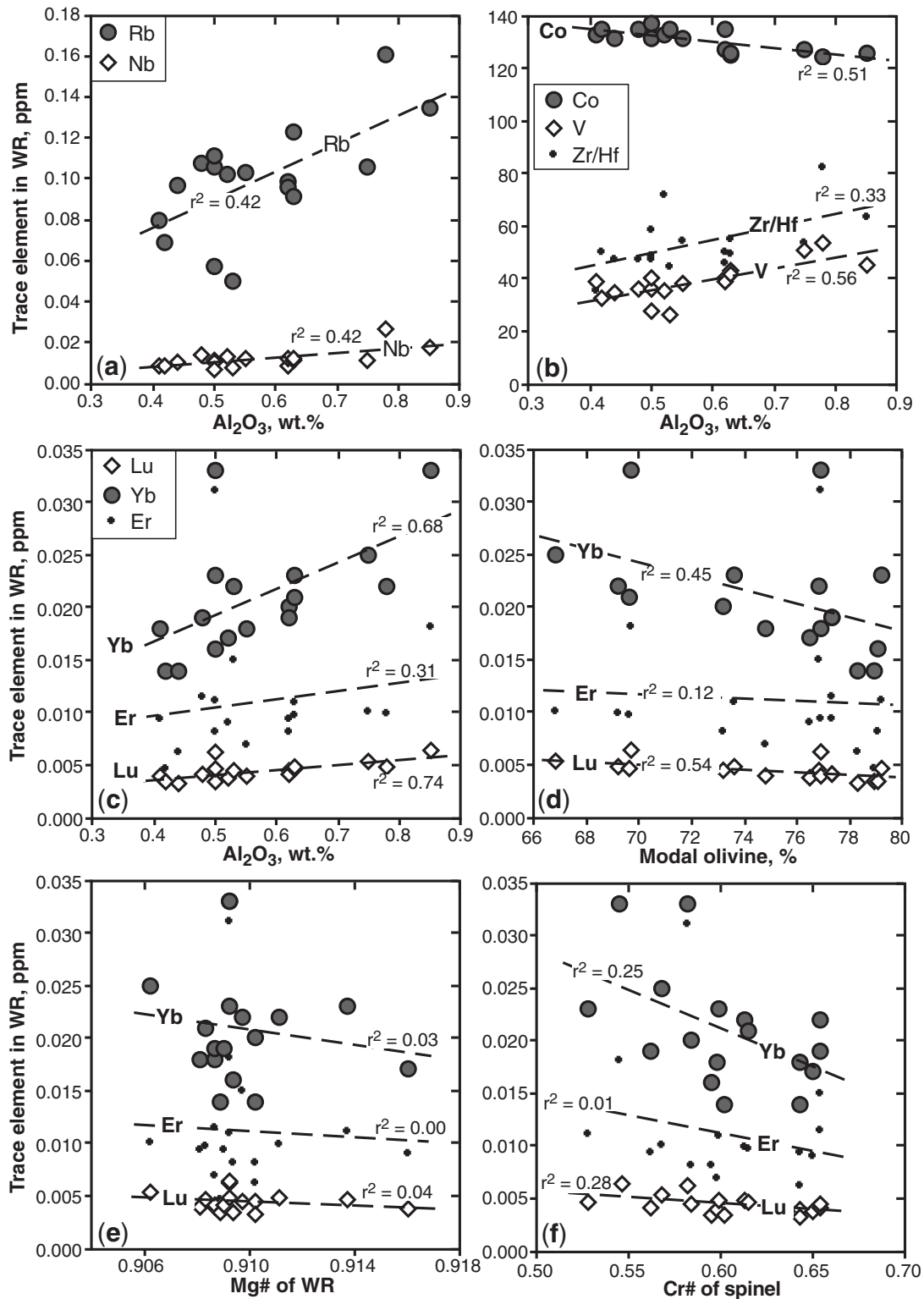


Fig. 17. (a–f) Plots of trace element contents (in ppm) and ratios in bulk-rock Avacha peridotites vs commonly used chemical or modal melt extraction indices. The contents of heavy REE, Co, V, Rb and Nb and Zr/Hf appear to be related to the melting indices, but not those of MREE (Er). The plots of bulk-rock Al_2O_3 and modal olivine yield the highest correlation coefficients whereas $\text{Mg}\#_{\text{WR}}$ and $\text{Cr}\#_{\text{sp}}$ do not appear to be robust indices of melt extraction degrees (see Fig. 7).

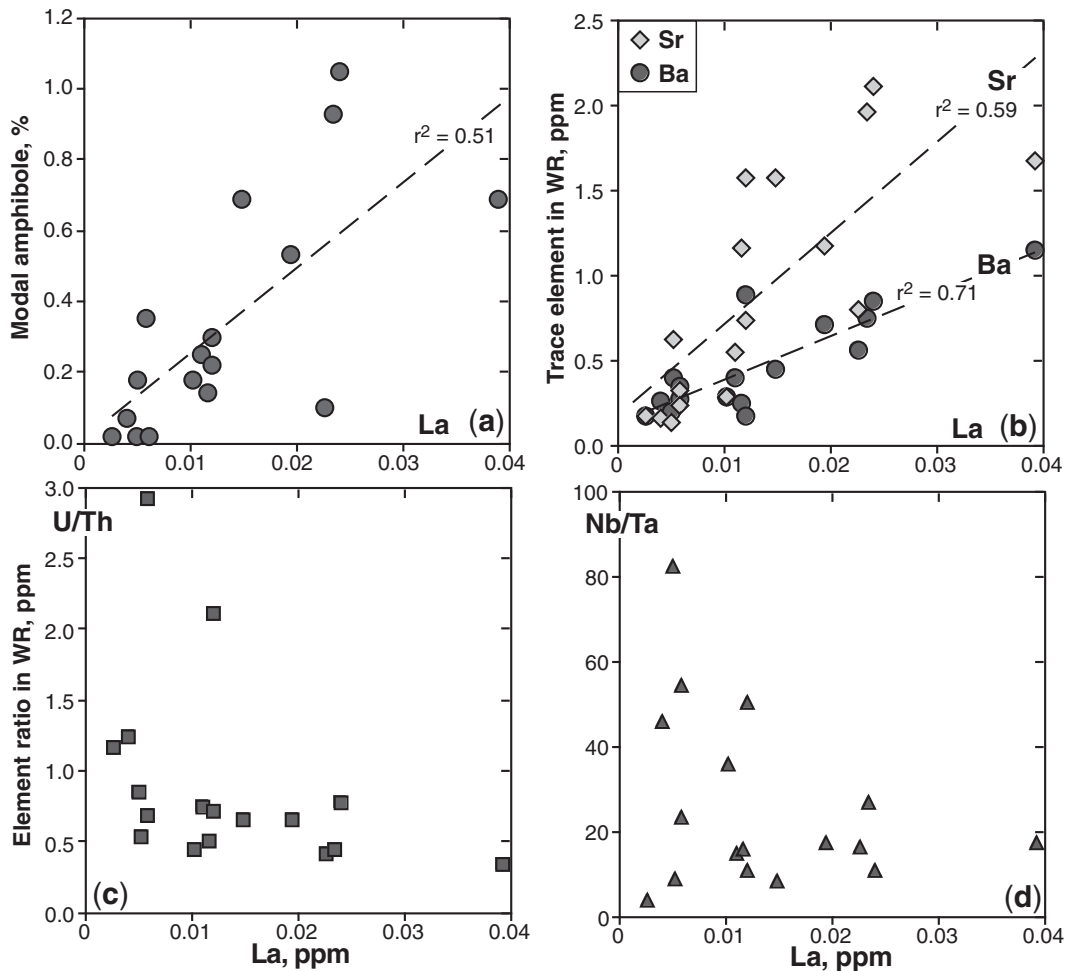


Fig. 18. (a–d) Plots of La vs modal amphibole (a), Sr and Ba abundances (b) and U/Th and Nb/Ta ratios (c, d) for bulk-rock Avacha peridotites. La contents are positively correlated with modal amphibole and those of Sr and Ba; high U/Th and Nb/Ta are found only in rocks with the lowest La.

is hard to test because of scarce experimental data, uncertainties in mantle source compositions (fertile asthenosphere to depleted oceanic lithosphere), the nature of the fluids involved (aqueous fluids, hydrous melts) and their compositions, and the complex, multi-stage nature of the melting processes (e.g. Grove *et al.*, 2006).

Post-melting fractionation and metasomatism in the source of the Avacha peridotites

An alternative explanation for the unusual modal and chemical characteristics of the Avacha suite, such as silica and opx enrichment, could be that they were produced after, rather than during, the initial partial melting event. Two mechanisms can be envisaged: (1) sorting of olivine and opx crystals in the unconsolidated melting residues or addition of cumulus opx (Herzberg, 1993); (2) selective metasomatic enrichment in SiO₂ by fluids to transform some olivine into opx.

The first mechanism could produce weak negative correlations between modal olivine and whole-rock CaO and Al₂O₃ (Fig. 14a), because the high-*T* opx in the residues is relatively rich in Ca and Al (e.g. Herzberg, 2004). Similarly, a negative Cr#_{Sp} vs whole-rock-Al₂O₃ trend (Fig. 13b) might be produced through re-equilibration between residual (or exsolved) Cr-spinel and variable amounts of Al-rich opx on cooling. Importantly, such a mechanism would yield much lower whole-rock Ca and Al contents (and no primary cpx) in the opx-rich peridotites compared with ‘dry’ partial melting residues at similar modal olivine contents (Figs 11 and 14). However, it is not clear why and how such processes would operate in the mantle wedge.

A mechanism for silica enrichment in ancient mantle wedge environments by fluids and melts expelled from subducted oceanic lithosphere has been proposed by several workers to explain modal opx variations in cratonic

mantle peridotites (e.g. Rudnick *et al.*, 1994; Kelemen *et al.*, 1998; Pearson & Wittig, 2008). Certain chemical trends within the Avacha suite (e.g. Mg–Si and Al–Si in Fig. 11b and d) partially overlap the compositional fields of cratonic peridotites and are distinct from those of younger continental lithosphere domains. Slab–wedge interaction could have been more intensive in the Archean because of higher mantle temperatures, and more common slab melting and active tectonics; this may have produced more extreme end-members than those seen in the trends for the Phanerozoic Avacha xenolith suite.

A major problem with this mechanism is that to be applicable to the Avacha suite it requires enrichment in silica alone, which rules out as potential metasomatic agents any silica-rich melt or fluid that contains significant amounts of Al, Ca, Fe, Ti, alkalis and fluid-mobile incompatible trace elements. This is particularly relevant in the context of the extremely low contents of Na in the Avacha whole-rocks and cpx, in comparison with the high solubility of alkalis in aqueous fluids. An alternative could be a two-stage process, with metasomatic silica enrichment followed by a minor melt extraction event to remove the highly fusible alkalis, Ti and Ca.

Whole-rock enrichments in silica and opx in the Avacha suite are restricted to samples with abundant coarse opx and have little, if anything, to do with secondary, fine-grained opx. Rather than being the main indices of subduction metasomatism, as proposed by Arai *et al.* (2003) and Ishimaru *et al.* (2007), the late-stage re-crystallization and related phenomena are only the latest, and probably least significant in terms of modal and major element variation, in a long sequence of events that affected the source region of the Avacha xenoliths. Regarding subduction-type metasomatism, its most important stage most probably takes place deeper in the mantle wedge; that is, much earlier and closer to sources of the fluids expelled from the subducted slab, when the source region of the Avacha peridotites was still part of mantle wedge asthenosphere.

Differences from previous studies of Avacha xenoliths

Several findings of this study and their interpretation differ from those reported by Ishimaru *et al.* (2007) on another suite of Avacha xenoliths. Some of the differences may stem from the focus of Ishimaru *et al.* (2007) on the most metasomatized peridotites and their late-stage components, whereas the objective of this study is to comprehensively characterize the petrology of peridotites typical of the mantle beneath Avacha. These differences and their relation to the origin of the Avacha peridotites are summarized below.

Petrography

This study finds no conclusive evidence that the formation of fine-grained materials in some of the Avacha peridotites is mainly due to replacement of primary olivine by metasomatic opx and thus represents a metasomatic event triggered by infiltration of SiO₂-rich fluids. The great majority of the fine-grained opx was formed after coarse opx (Figs 4c, d and 6). Small-scale replacement of olivine by opx did take place locally, but the fine-grained materials also include olivine neoblasts formed after opx (Fig. 6c and d). The net effects of these complementary processes cannot be assessed from textural observations on small-scale features alone and have to be explored using bulk-rock compositions (see below).

The great majority of the late-stage, fine-grained opx in the Avacha xenoliths from this study are anhedral or prismatic; the latter grains are usually sub-parallel to the cleavage of the coarse opx which they replace (Figs 4c and 6a). No ‘fibrous’ opx has been found; ‘radially aggregated’ opx and silicate glass (Ishimaru & Arai, 2009) are very rare in the xenoliths from this study. There is no evidence that such features can be viewed as indicative of ‘subduction-type’ metasomatism; they were probably produced shortly before the eruption that carried the xenoliths to the surface in the shallow mantle infiltrated by the host andesitic magmas and their derivatives.

Importantly, this study finds no correlation between whole-rock abundances of SiO₂ or modal opx and the proportion of the fine-grained materials. Xenolith Av4 has the highest silica (45.2%) and modal opx (30%) among the Avacha samples from this study, but contains practically no secondary opx (Figs 3c and 4a); by contrast, mainly fine-grained xenoliths Av1 and Av16 (Fig. 3e–h) and xenolith Av9 with common secondary opx (Fig. 4d) are low both in silica (43.4–44%) and in opx (18–20%). The Avacha peridotites cannot be grouped into ‘primary’ and ‘metasomatic’ based on the presence or contents of fine-grained opx or amphibole; the latter mineral is present in nearly all the xenoliths ($\leq 1\%$).

Chemical and modal compositions

Significant differences in the contents of some oxides between the Avacha xenoliths in this study and those reported by Ishimaru *et al.* (2007) are seen in Figs 11 and 12. In particular, the SiO₂ contents in the dataset of Ishimaru *et al.* (2007) are 1–3% lower at a given Al₂O₃ or MgO content such that they plot below the co-variation trends defined by various other mantle peridotites and the experimental data of Herzberg (2004) in Fig. 12b and d. Thus the inference of Ishimaru *et al.* (2007) that their xenolith suite experienced post-melting metasomatic enrichment in silica is not supported by their own bulk-rock data. The contents of FeO and MgO tend to be higher and Mg# lower, whereas NiO contents are extremely

variable (Fig. 11a) compared with the data from this study. Unlike the data from this study, Ishimaru *et al.* (2007) reported neither LOI data nor analyses of duplicates and reference samples; their analyses have highly variable but systematically low totals (96.2–99.0%).

Hypothetical addition of an FeO-rich agent with high Fe/Mg during partial melting or metasomatism (Ishimaru *et al.*, 2007) is not supported by the bulk-rock data from this study (Fig. 11f) and the absence of Fe-enrichment in the rims of olivine and opx. The Avacha peridotites define a negative correlation between SiO₂ and FeO, which should be the opposite in case of ingress of melts rich both in Fe and Si.

Modal olivine abundances reported by Ishimaru *et al.* (2007) are generally higher than in this study and show no correlation with whole-rock Al₂O₃ and CaO (Fig. 14a and b) but define an unlikely negative correlation with Mg#_{O1} (Fig. 14c). This may be due to uncertainties in the point-counting technique of those workers as a result of modal heterogeneities and difficulties in distinguishing fine-grained olivine and opx in thin section.

The Avacha samples from this study and those reported in table 4 of Ishimaru *et al.* (2007) show no statistically meaningful Mg#_{O1}–Cr#_{Spl} correlation, which disagrees with the claim of those workers that their samples define an unusual negative Mg#_{O1}–Cr#_{Spl} trend [‘Avacha trend’ in fig. 9 of Ishimaru *et al.* (2007)]. In general, refractory peridotites with Cr#_{Spl} > 0.5 rarely show clear-cut Mg#_{O1}–Cr#_{Spl} trends, either in single suites or in data compilations, possibly because of common late-stage Fe enrichment and differences in melting depth and tectonic setting (e.g. Ionov *et al.*, 2005b; Ionov & Hofmann, 2007); the Avacha suite does not seem to be unusual in this regard.

SUMMARY OF CONCLUSIONS

- (1) The Avacha peridotite xenolith suite from this study consists of highly refractory harzburgites, extremely poor in alkalis and Ti, with fairly uniform modal, bulk-rock and mineral compositions.
- (2) Some Avacha peridotites show bulk-rock enrichment in silica and plot off co-variation trends defined by continental off-craton and ocean island xenoliths, as well as experimental melting residues on Mg–Al–Si diagrams. A distinctive feature of the Avacha suite, and possibly other supra-subduction zone peridotites, is the combination of variable, but commonly high, modal opx (18–30%) with very low modal cpx.
- (3) The Al–Fe–Mg relations and HREE abundances are consistent with extraction of 28–35% of mafic melts from fertile mantle at ≤ 1 to 2 GPa to yield cpx-free residues. This melting may have involved several stages, possibly including flux melting in the mantle

wedge to form a uniformly refractory residual peridotite.

- (4) The melting residues were incorporated into the lithosphere and experienced long-term slow cooling to at least 900–1000°C. The cooling resulted in exsolution of cpx and spinel from high-*T* residual opx and affected the composition of the residual spinel. Percolation of alkali-poor hydrous fluids through the lithosphere produced variable, but generally small, amounts of amphibole (≤ 1%) and minor enrichments in incompatible elements.
- (5) Shortly before the transport of the xenoliths to the surface some of them experienced fracturing and re-crystallization to form thin veins and fine-grained pockets (mainly replacing coarse opx) without significant effects on bulk-rock modal and major element compositions.

ACKNOWLEDGEMENTS

I am grateful to G. Brey, A. Hofmann and D. Weis for support in Frankfurt, Mainz and Brussels, and to J.-Y. Jolivel and other participants of the excursion to Kamchatka in 2002. Analytical and technical assistance was provided by A. Friedrichsen, N. Groschopf, A. Gurenko, J. Heliosch, H. Höfer, T. Kautz, D. Kuzmin, Y. Lahaye and C. Merlet (Microsonde Sud). The manuscript benefited from comments by S. Arai, M. Coltorti, L. Frantz and two anonymous reviewers; editorial handling by M. Wilson is much appreciated.

FUNDING

The research was supported by funding from Centre National de la Recherche Scientifique (CNRS) (France) including a SEDIT project in 2008, Max-Planck-Society and Deutsche Forschungsgemeinschaft (DFG) (Germany), including a DFG Mercator Guest Professorship in 2005–2006.

SUPPLEMENTARY DATA

Supplementary data for this paper are available at *Journal of Petrology* online.

REFERENCES

- Arai, S., Ishimaru, S. & Okrugin, V. M. (2003). Metasomatized harzburgite xenoliths from Avacha volcano as fragments of mantle wedge of the Kamchatka arc: Implication for the metasomatic agent. *Island Arc* **12**, 233–246.
- Avdeiko, G. P., Popruzhenko, S. V. & Palueva, A. A. (2002). The tectonic evolution and volcano-tectonic zonation of the Kuril–Kamchatka island-arc system. *Geotectonics* **36**, 312–327.
- Ballhaus, C., Berry, R. F. & Green, D. H. (1991). High pressure experimental calibration of the olivine–orthopyroxene–spinel oxygen

- geobarometer: implications for the oxidation state of the upper mantle. *Contributions to Mineralogy and Petrology* **107**, 27–40.
- Barsdell, M. & Smith, I. E. M. (1989). Petrology of recrystallized ultramafic xenoliths from Merelava volcano, Vanuatu. *Contributions to Mineralogy and Petrology* **102**, 230–241.
- Bird, P. (2003). An updated digital model of plate boundaries. *Geochemistry, Geophysics, Geosystems* **4**, 1027, doi:10.1029/2001GC000252.
- Bodinier, J.-L. & Godard, M. (2003). Orogenic, ophiolitic and abyssal peridotites. In: Carlson, R. W. (ed.) *Treatise on Geochemistry. Vol. 2. The Mantle and Core*. Amsterdam: Elsevier, pp. 103–170.
- Bonadiman, C., Beccaluva, L., Coltorti, M. & Siena, F. (2005). Kimberlite-like metasomatism and 'garnet signature' in spinel-peridotite xenoliths from Sal, Cape Verde archipelago: relics of a subcontinental mantle domain within the Atlantic oceanic lithosphere? *Journal of Petrology* **46**, 2465–2493.
- Boyd, F. R., Pokhilenko, N. P., Pearson, D. G., Mertzman, S. A., Sobolev, N. V. & Finger, L. W. (1997). Composition of the Siberian cratonic mantle: evidence from Udachnaya peridotite xenoliths. *Contributions to Mineralogy and Petrology* **128**, 228–246.
- Braitseva, O. A., Bazanova, L. I., Melekestsev, I. V. & Sulerzhitskiy, L. D. (1998). Large Holocene eruptions of Avacha volcano, Kamchatka (7250–3700 ¹⁴C years B.P.). *Volcanology and Seismology* **20**, 1–27.
- Brey, G. P. & Köhler, T. (1990). Geothermobarometry in four-phase lherzolites II. New thermobarometers, and practical assessment of existing thermobarometers. *Journal of Petrology* **31**, 1353–1378.
- Bryant, J. A., Yagodinski, G. M. & Churikova, T. G. (2007). Melt-mantle interactions beneath the Kamchatka arc: Evidence from ultramafic xenoliths from Shiveluch volcano. *Geochemistry, Geophysics, Geosystems* **8**, Q04007, doi:10.1029/2006GC001443.
- Bryndzia, T. L., Wood, B. J. & Dick, H. J. B. (1989). The oxidation state of the Earth's sub-oceanic mantle from oxygen thermobarometry of abyssal spinel peridotites. *Nature* **341**, 526–527.
- Coltorti, M., Bonadiman, C., Faccini, B., Grégoire, M., O'Reilly, S. Y. & Powell, W. (2007). Amphiboles from suprasubduction and intra-plate lithospheric mantle. *Lithos* **99**, 68–84.
- Franz, L., Becker, K.-P., Kramer, W. & Herzig, P. M. (2002). Metasomatic mantle xenoliths from the Bismarck Microplate (Papua New Guinea)—thermal evolution, geochemistry and extent of slab-induced metasomatism. *Journal of Petrology* **43**, 315–343.
- Godard, M., Lagabrielle, Y., Alard, O. & Harvey, J. (2008). Geochemistry of the highly depleted peridotites drilled at ODP Sites 1272 and 1274 (Fifteen–Twenty Fracture Zone, Mid-Atlantic Ridge): Implications for mantle dynamics beneath a slow spreading ridge. *Earth and Planetary Science Letters* **267**, 410–425.
- Gorbatov, A., Kostoglodov, V., Suárez, G. & Gordeev, E. (1997). Seismicity and structure of the Kamchatka subduction zone. *Journal of Geophysical Research* **102**, 17883–17898.
- Gorbatov, A., Dominguez, J., Suarez, G., Kostoglodov, V., Zhao, D. & Gordeev, E. (1999). Tomographic imaging of the P-wave velocity structure beneath the Kamchatka peninsula. *Geophysical Journal International* **137**, 269–279.
- Gorbatov, A., Widiyantoro, S., Fukao, Y. & Gordeev, E. (2000). Signature of remnant slabs in the North Pacific from P-wave tomography. *Geophysical Journal International* **142**, 27–36.
- Grove, T. L., Chatterjee, N., Parman, S. W. & Medard, E. (2006). The influence of H₂O on mantle wedge melting. *Earth and Planetary Science Letters* **249**, 74–89.
- Hart, S. R. & Zindler, A. (1986). In search of a bulk-Earth composition. *Chemical Geology* **57**, 247–267.
- Herzberg, C. (2004). Geodynamic information in peridotite petrology. *Journal of Petrology* **45**, 2507–2530.
- Herzberg, C. T. (1993). Lithosphere peridotites of the Kaapvaal craton. *Earth and Planetary Science Letters* **120**, 13–29.
- Hirose, K. & Kawamoto, T. (1995). Hydrous partial melting of lherzolite at 1 GPa: the effect of H₂O on the genesis of basaltic magmas. *Earth and Planetary Science Letters* **133**, 463–473.
- Hirschmann, M. M., Baker, M. B. & Stolper, E. M. (1998). The effect of alkalis on the silica content of mantle-derived melts. *Geochimica et Cosmochimica Acta* **62**, 883–902.
- Hofmann, A. W. (1988). Chemical differentiation of the Earth: the relationship between mantle, continental crust, and oceanic crust. *Earth and Planetary Science Letters* **90**, 297–314.
- Ionov, D. A. (2004). Chemical variations in peridotite xenoliths from Vitim, Siberia: inferences for REE and Hf behaviour in the garnet-facies upper mantle. *Journal of Petrology* **45**, 343–367.
- Ionov, D. A. (2007). Compositional variations and heterogeneity in fertile lithospheric mantle: peridotite xenoliths in basalts from Tariat, Mongolia. *Contributions to Mineralogy and Petrology* **154**, 455–477.
- Ionov, D. A. & Hofmann, A. W. (2007). Depth of formation of subcontinental off-craton peridotites. *Earth and Planetary Science Letters* **261**, 620–634.
- Ionov, D. A. & Seitz, H. M. (2008). Lithium abundances and isotopic compositions in mantle xenoliths from subduction and intra-plate settings: mantle sources versus eruption histories. *Earth and Planetary Science Letters* **266**, 316–331.
- Ionov, D. A. & Wood, B. J. (1992). The oxidation state of subcontinental mantle: oxygen thermobarometry of mantle xenoliths from central Asia. *Contributions to Mineralogy and Petrology* **111**, 179–193.
- Ionov, D. A., O'Reilly, S. Y. & Griffin, W. L. (1997). Volatile-bearing minerals and lithophile trace elements in the upper mantle. *Chemical Geology* **141**, 153–184.
- Ionov, D. A., O'Reilly, S. Y. & Griffin, W. L. (1998). A geotherm and lithospheric cross-section for central Mongolia. In: Flower, M. J. F., Chung, S.-L. & Lo, C.-H. *et al.* (eds) *Mantle Dynamics and Plate Interactions in East Asia*. American Geophysical Union, *Geodynamics Series* **27**, 127–153.
- Ionov, D. A., Bodinier, J.-L., Mukasa, S. B. & Zanetti, A. (2002). Mechanisms and sources of mantle metasomatism: major and trace element compositions of peridotite xenoliths from Spitsbergen in the context of numerical modeling. *Journal of Petrology* **43**, 2219–2259.
- Ionov, D. A., Ashchepkov, I. & Jagoutz, E. (2005a). The provenance of fertile off-craton lithospheric mantle: Sr–Nd isotope and chemical composition of garnet and spinel peridotite xenoliths from Vitim, Siberia. *Chemical Geology* **217**, 41–75.
- Ionov, D. A., Chanefo, I. & Bodinier, J.-L. (2005b). Origin of Fe-rich lherzolites and wehrlites from Tok, SE Siberia by reactive melt percolation in refractory mantle peridotites. *Contributions to Mineralogy and Petrology* **150**, 335–353.
- Ionov, D. A., Prikhodko, V. S., Bodinier, J.-L., Sobolev, A. V. & Weis, D. (2005c). Lithospheric mantle beneath the south-eastern Siberian craton: petrology of peridotite xenoliths in basalts from the Tokinsky Stanovik. *Contributions to Mineralogy and Petrology* **149**, 647–665.
- Ishimaru, S. & Arai, S. (2008). Calcic amphiboles in peridotite xenoliths from Avacha volcano, Kamchatka, and their implications for metasomatic conditions in the mantle wedge. In: Coltorti, M. & Grégoire, M. (eds) *Metasomatism in Oceanic and Continental Lithospheric Mantle*. Geological Society, London, *Special Publications* **293**, 35–55.

- Ishimaru, S. & Arai, S. (2009). Highly silicic glasses in peridotite xenoliths from Avacha volcano, Kamchatka arc; implications for melting and metasomatism within the sub-arc mantle. *Lithos* **107**, 93–106.
- Ishimaru, S., Arai, S., Ishida, Y., Shirasaka, M. & Okrugin, V. M. (2007). Melting and multi-stage metasomatism in the mantle wedge beneath a frontal arc inferred from highly depleted peridotite xenoliths from the Avacha volcano, southern Kamchatka. *Journal of Petrology* **48**, 395–433.
- Jarosewich, E., Nelen, J. A. & Norberg, J. (1980). Reference samples for electron microprobe analysis. *Geostandards Newsletter* **4**, 43–47.
- Kelemen, P. B. (1990). Reaction between ultramafic wall rock and fractionating basaltic magma: Part I, Phase relations, the origin of calc-alkaline magma series, and the formation of discordant dunite. *Journal of Petrology* **31**, 51–98.
- Kelemen, P. B., Hart, S. R. & Bernstein, S. (1998). Silica enrichment in the continental upper mantle via melt/rock reaction. *Earth and Planetary Science Letters* **164**, 387–406.
- Kepezhinskas, P., Defant, M. J. & Widom, E. (2002). Abundance and distribution of PGE and Au in the island-arc mantle: implications for sub-arc metasomatism. *Lithos* **60**, 113–128.
- Kepezhinskas, P. K., Defant, M. J. & Drummond, M. S. (1996). Progressive enrichment of island arc mantle by melt–peridotite interaction inferred from Kamchatka xenoliths. *Geochimica et Cosmochimica Acta* **60**, 1217–1229.
- Köhler, T. P. & Brey, G. P. (1990). Calcium exchange between olivine and clinopyroxene calibrated as a geothermobarometer for natural peridotites from 2 to 60 kb with applications. *Geochimica et Cosmochimica Acta* **54**, 2375–2388.
- Levin, V., Park, J., Brandon, M., Lees, J., Peyton, V., Gordeev, E. & Ozerov, A. (2002). Crust and upper mantle of Kamchatka from teleseismic receiver functions. *Tectonophysics* **358**, 233–265.
- Levin, V., Droznin, D., Park, J. & Gordeev, E. (2004). Detailed mapping of seismic anisotropy with local shear waves in southeastern Kamchatka. *Geophysical Journal International* **158**, 1009–1023.
- Manea, V. C., Manea, M., Kostoglodov, V. & Sewell, G. (2005). Thermal models, magma transport and velocity anomaly estimation beneath southern Kamchatka. In: Foulger, G. R., Natland, J. H. & Presnall, D. C. *et al.* (eds) *Plates, Plumes, and Paradigms*. *Geological Society of America, Special Papers* **388**, 517–536.
- Maury, R. C., Defant, M. J. & Joron, J.-L. (1992). Metasomatism of the sub-arc mantle inferred from trace elements in Philippine xenoliths. *Nature* **360**, 661–663.
- McDonough, W. F. & Sun, S.-s. (1995). The composition of the Earth. *Chemical Geology* **120**, 223–253.
- McInnes, B. I. A., Grégoire, M., Binns, R. A., Herzig, P. M. & Hannington, M. D. (2001). Hydrous metasomatism of oceanic sub-arc mantle, Lihir, Papua New Guinea: petrology and geochemistry of fluid-metasomatised mantle wedge xenoliths. *Earth and Planetary Science Letters* **188**, 169–183.
- Miller, M. S. & Kennett, B. L. N. (2006). Evolution of mantle structure beneath the northwest Pacific: Evidence from seismic tomography and paleogeographic reconstructions. *Tectonics* **25**, TC4002, doi:10.1029/2005TC001909.
- Neumann, E.-R. & Simon, N. S. C. (2009). Ultra-refractory mantle xenoliths from ocean islands: How do they compare to peridotites retrieved from oceanic sub-arc mantle? *Lithos* **107**, 1–16.
- Neumann, E.-R., Wulff-Pedersen, E., Pearson, N. J. & Spenser, E. A. (2002). Mantle xenoliths from Tenerife (Canary Islands): evidence for reactions between mantle peridotites and silicic carbonate melts inducing Ca metasomatism. *Journal of Petrology* **43**, 825–857.
- Niu, Y. (2004). Bulk-rock major and trace element compositions of abyssal peridotites: implications for mantle melting, melt extraction and post-melting processes beneath mid-ocean ridges. *Journal of Petrology* **45**, 2423–2458.
- Palme, H. & O'Neill, H. S. C. (2003). Cosmochemical estimates of mantle composition. In: Carlson, R. W. (ed.) *Treatise on Geochemistry. Vol. 2. The Mantle and Core*. Amsterdam: Elsevier, pp. 1–38.
- Parkinson, I. J. & Pearce, J. A. (1998). Peridotites from the Izu–Bonin–Mariana forearc (ODP Leg 125): evidence for mantle melting and melt–mantle interaction in a supra-subduction zone setting. *Journal of Petrology* **39**, 1577–1618.
- Parkinson, I. J., Arculus, R. J. & Eggins, S. M. (2003). Peridotite xenoliths from Grenada, Lesser Antilles Island Arc. *Contributions to Mineralogy and Petrology* **146**, 241–262.
- Pearson, D. G. & Wittig, N. (2008). Formation of Archaean continental lithosphere and its diamonds: the root of the problem. *Journal of the Geological Society of London* **165**, 895–914.
- Pearson, D. G., Canil, D. & Shirey, S. B. (2003). Mantle samples included in volcanic rocks: xenoliths and diamonds. In: Carlson, R. W. (ed.) *Treatise on Geochemistry. Vol. 2. The Mantle and Core*. Amsterdam: Elsevier, pp. 171–276.
- Rudnick, R. L., McDonough, W. F. & Orpin, A. (1994). Northern Tanzanian peridotite xenoliths: A comparison with Kaapvaal peridotites and inferences on metasomatic interactions. In: Meyer, H. O. A. & Leonardos, O. (eds) *Kimberlites, Related Rocks and Mantle Xenoliths. Proceedings of the 5th International Kimberlite Conference* **1**, Brasilia: CPRM, pp. 336–353.
- Saha, A., Basu, A. R., Jacobsen, S. B., Poreda, R. J., Yin, Q.-Z. & Yogodzinski, G. M. (2005). Slab devolatilization and Os and Pb mobility in the mantle wedge of the Kamchatka arc. *Earth and Planetary Science Letters* **236**, 182–194.
- Simon, N. S. C., Irvine, G. J., Davies, G. R., Pearson, D. G. & Carlson, R. W. (2003). The origin of garnet and clinopyroxene in ‘depleted’ Kaapvaal peridotites. *Lithos* **71**, 289–322.
- Simon, N. S. C., Neumann, E.-R., Bonadiman, C., Coltorti, M., Delpech, G., Grégoire, M. & Widom, E. (2008). Ultra-refractory domains in the oceanic mantle lithosphere sampled as mantle xenoliths at ocean islands. *Journal of Petrology* **49**, 1223–1251.
- Sobolev, A. V., Hofmann, A. W., Sobolev, S. V. & Nikogosian, I. K. (2005). An olivine-free mantle source of Hawaiian shield basalts. *Nature* **434**, 590–597.
- Soustelle, V., Tommasi, A., Demouchy, S. & Ionov, D. A. (2010). Deformation and fluid-rock interaction in the supra-subduction zone mantle: Microstructures and water contents in peridotite xenoliths from the Avacha Volcano, Kamchatka. *Journal of Petrology* **51**, 363–394.
- Stern, R. J. (2002). Subduction zones. *Reviews of Geophysics* **40**, 1012, doi:10.1029/2001RG000108.
- Swanson, S. E., Kay, S. M., Brearley, M. & Scarfe, C. M. (1987). Arc and back-arc xenoliths in Kurile–Kamchatka and western Alaska. In: Nixon, P. H. (ed.) *Mantle Xenoliths*. Chichester: John Wiley, pp. 303–318.
- Takahashi, E. (1980). Thermal history of lherzolite xenoliths—I. Petrology of lherzolite xenoliths from the Ichinomegata Crater, Oga Peninsula, northeast Japan. *Geochimica et Cosmochimica Acta* **44**, 1643–1658.
- Takahashi, E. (1986). Genesis of calc-alkali andesite magma in a hydrous mantle–crust boundary: Petrology of lherzolite xenoliths from the Ichinomegata Crater, Oga Peninsula, northeast Japan, part II. *Journal of Volcanology and Geothermal Research* **29**, 355–395.
- Takazawa, E., Frey, F. A., Shimizu, N. & Obata, M. (2000). Whole rock compositional variations in an upper mantle peridotite

- (Horoman, Hokkaido, Japan): Are they consistent with a partial melting process. *Geochimica et Cosmochimica Acta* **64**, 695–716.
- van Keken, P. E. (2003). The structure and dynamics of the mantle wedge. *Earth and Planetary Science Letters* **215**, 323–338.
- Vidal, P., Dupuy, C., Maury, R. & Richard, M. (1989). Mantle metasomatism above subduction zones: Trace-element and radiogenic isotope characteristics of peridotite xenoliths from Batan Island (Philippines). *Geology* **17**, 1115–1118.
- Walter, M. J. (2003). Melt extraction and compositional variability in mantle lithosphere. In: Carlson, R. W. (ed.) *Treatise on Geochemistry*. Vol. 2. *The Mantle and Core*. Amsterdam: Elsevier, pp. 363–394.
- Webb, S. A. C. & Wood, B. J. (1986). Spinel–pyroxene–garnet relationships and their dependence on Cr/Al ratio. *Contributions to Mineralogy and Petrology* **92**, 471–480.
- Weyer, S. & Ionov, D. A. (2007). Partial melting and melt percolation in the mantle: The message from Fe isotopes. *Earth and Planetary Science Letters* **259**, 119–133.
- Widom, E., Kepezhinskas, P. & Defant, M. J. (2003). The nature of metasomatism in the sub-arc mantle wedge: evidence from Re–Os isotopes in Kamchatka peridotite xenoliths. *Chemical Geology* **196**, 283–306.
- Wiechert, U., Ionov, D. A. & Wedepohl, K. H. (1997). Spinel peridotite xenoliths from the Atsagin-Dush volcano, Dariganga lava plateau, Mongolia: A record of partial melting and cryptic metasomatism in the upper mantle. *Contributions to Mineralogy and Petrology* **126**, 345–364.
- Witt-Eickschen, G. & O'Neill, H. S. C. (2005). The effect of temperature on the equilibrium distribution of trace elements between clinopyroxene, orthopyroxene, olivine and spinel in upper mantle peridotite. *Chemical Geology* **221**, 65–101.
- Wood, B. J. (1991). Oxygen barometry of spinel peridotites. In: Lindsley, D. H. (ed.) *Oxide Minerals: Petrologic and Magnetic Significance*. Mineralogical Society of America, *Reviews in Mineralogy* **25**, 417–431.